Apparatus for the study of Rayleigh-Bénard convection in gases under pressure

John R. de Bruyn
Department of Physics
Memorial University of Newfoundland
St. John's, Newfoundland, Canada A1B 3X7

Eberhard Bodenschatz
Department of Physics and Laboratory of Atomic and Solid State Physics
Cornell University
Ithaca, New York 14853

Stephen W. Morris
Department of Physics and Erindale College
University of Toronto
60 St. George St.,
Toronto, Ontario, Canada M5S 1A7

Steven P. Trainoff
Department of Physics and Center for Nonlinear Science
University of California
Santa Barbara, California 93106-9530

Yuchou Hu
Department of Physics and Center for Nonlinear Science
University of California
Santa Barbara, California 93106-9530
and
Center for Nonlinear Studies and Material Science and Technology Division
Los Alamos National Laboratory
Los Alamos, New Mexico 87545

David S. Cannell and Guenter Ahlers
Department of Physics and Center for Nonlinear Science
University of California
Santa Barbara, California 93106-9530
(October 13, 1997)

We review the history of experimental work on Rayleigh-Bénard convection in gases, and then describe a modern apparatus which has been used in our experiments on gas convection. This system allows the study of patterns in a cell with an aspect ratio (cell radius/fluid layer depth) as large as 100, with the cell thickness uniform to a fraction of a μm, and with the pressure controlled at the level of one part in 10^5. This level of control can yield a stability of the critical temperature difference for the convective onset of better than one part in 10^4. The convection patterns are visualized and the temperature field can be inferred using the shadowgraph technique. We describe the flow visualization and image processing necessary for this. Some interesting results obtained with the system are briefly summarized.

I. INTRODUCTION

When a spatially extended system is driven far from equilibrium by subjecting it to a stress, it will often undergo a transition from a spatially uniform state to a state with spatial variation. We refer to this variation as a "pattern". Pattern formation is generally associated with *nonlinear* effects. These are of great fundamental interest in the physical sciences as well as in engineering because they can lead to qualitatively new phenomena which do not occur in linear systems. Many of the phenomena encountered are common to a range of different systems, be they physical, chemical, or biological in nature [1]. For instance, depending on the parameter ranges, elongated structures known as "stripes" or "rolls", hexagonal patterns, and "turbulent" states are found in all of them. A scientist interested in the fundamental aspects of these ubiquitous effects will choose a particular system which is well suited to detailed, quantitative study. With this aim in mind, we have examined fundamental aspects of pattern formation by conducting experiments on fluid systems. In particular, we investigated several variations of the simple problem of a thin horizontal fluid layer heated from below. The convection which occurs when the temperature difference across the layer is sufficiently large is known as Rayleigh-Bénard convection(RBC) [2]. The fluid flow associated with it forms a pattern. It offers exceptional opportunities to the experimentalist, and has been used for several decades to investigate a number of fundamental nonlinear phenomena [3]. Problems which have been examined *quantitatively* in more recent years are the formation of patterns consisting of rolls, hexagons, and spirals, the existence of coherent structures consisting of pulses of convection rolls, the influence of noise associated with the finite temperature of the system on the pattern-formation process, and the evolution of irregular time dependence which eventually leads to a turbulent state [1,4]. For much of this work, convection in a layer of a compressed gas has been particularly suitable. In the present paper we review the history of gas convection and our experiences in building suitable apparatus for its quantitative study.

The basic idea of RBC is illustrated in Fig. 1. A thin horizontal layer of fluid is heated from below by an external heater, setting up a temperature gradient across the layer. As a result of thermal expansion and the finite thermal conductivity, a potentially unstable stratification develops: the fluid at the bottom of the layer is warmer, and hence less dense, than the fluid at the top of the layer. When the gravitational potential energy gained by moving the lighter fluid from the bottom to the top of the layer, and replacing it with the heavier fluid, outweighs the energy lost to viscous dissipation and thermal diffusion, the quiescent fluid layer becomes unstable and a convective flow appears. This flow transports heat across the layer, in excess of that transported by thermal conduction with no flow. Under idealized experimental conditions, the convection appears in the form of long straight rolls, which are viewed end-on in Fig. 1. As the temperature difference across the layer is increased, these straight rolls can themselves become unstable, resulting in the appearance of different, and generally more complex flow patterns, the precise nature of which depends on the fluid properties and the experimental configuration. Eventually the pattern will become time dependent, and, ultimately, turbulent.
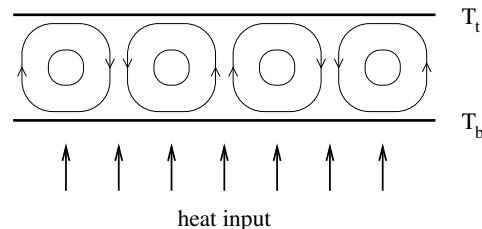

FIG. 1. A schematic illustration of Rayleigh-Bénard convection. A thin layer of fluid — in our case, a compressed gas — is confined between two parallel, horizontal rigid plates, and heat is applied to the system from below. The top plate is at temperature T_t and the bottom plate at temperature $T_b = T_t + \Delta T$. Because of the thermal expansion of the fluid, it is less dense near the bottom plate and more dense near the top. At a critical value of the temperature difference across the layer, ΔT_c, this unstable density gradient becomes large enough that a convective flow sets in, as illustrated.

Experimentally, convection patterns can be studied in a number of ways. A great deal of information, both qualitative and quantitative, can be obtained by actually visualizing the convective flow, particularly when the planform of the flow is viewed from above. Several flow-visualization techniques have been used, including tracer particles, interferometry, and shadowgraphs. Heat transport across the layer can be measured, as can local temperatures within the layer. The local flow velocity can be measured using techniques such as laser-Doppler velocimetry. Some measurement techniques are less satisfactory than others, in that they are invasive — the introduction of tracer particles or thermocouples into the convecting fluid might affect the flow pattern being measured. Our own work has primarily relied on the shadowgraph method [5–15] as a noninvasive technique for the visualization of convective flow patterns.

Experimental studies of RBC have been carried out using many different fluids, including water, silicone oil, ethanol-water mixtures, liquid helium, nematic liquid crystals, and liquid metals. Each of them covers some particular parameter range of interest, and carefully designed experiments on these have yielded many important results [1,3,4,6,16–20]. The range of parameter space accessible by using a gas is very different from that probed by using liquids. In part this is because the dissipation by heat diffusion and by viscosity is about equally important in gases, whereas viscosity dominates in ordi-

nary liquids and heat diffusion is most important in liquid metals. The instabilities of the straight convection rolls, the onset of time dependence, and the resulting dynamics of the convection patterns above onset are quite different in gases than in, say, water or silicone oil [21–27]. The study of convection in gases has a long history which we will review in Sect. 3. In recent years it has seen a revival primarily due to the work of Croquette, Pocheau, and co-workers, [12,28–30] and to that of our group. Recent experiments using the apparatus described in Section IV of this paper have uncovered new and unexpected phenomena which have added to our understanding of some of the questions raised above, as well as raising other, new issues [31–44].

The remainder of this paper is organized as follows. In Section II, we introduce RBC in more detail, with emphasis on the features of the system which make it so well suited for the study of patterns, and on those points specific to convection in gases which have a bearing on the design of the apparatus. Previous work on RBC in gases is reviewed in Section III. Our own apparatus is described in Section IV. It has a convection cell of large aspect ratio which is uniform in thickness to optical precision, has sub-milli-Kelvin temperature control, pressure control at the level of one part in 10^5, and uses ultra-high-resolution shadowgraph flow visualization. In Section V, we present some typical results from our recent experiments [31–44], and comment on possible future directions for research in this area.

II. RAYLEIGH-BÉNARD CONVECTION

There are a number of reasons — both experimental and theoretical — for the usefulness of RBC as a laboratory system for the study of the formation and dynamics of patterns. The equations describing RBC are well known. They are the Navier-Stokes equations of fluid flow, coupled with an equation for the heat transport across the fluid layer. Equally well defined are the boundary conditions for the temperature and velocities. Usually, the fluid is bounded above and below by rigid plates which are, to a good approximation, isothermal. The important properties of the convecting fluid and the experimental cell are usually known, or measurable, to a high accuracy, and convection cells with a very high degree of geometrical perfection have been constructed. Of particular importance is the fact that a systematic nonlinear stability analysis of the straight rolls which form initially [45–47] in RBC has been carried out by Busse and Clever [21–27], which makes predictions concerning the instabilities of straight rolls well above the convective onset. This is in contrast to the theoretical situation for many other pattern-forming systems, where in some cases the equations of motion are known only approximately and in others not at all. Even in favorable circumstances, usually little is known beyond the linear

approximation. The relatively advanced state of theoretical knowledge for RBC makes it possible to draw detailed comparisons between experimental results and theoretical predictions, sometimes at the 0.1% level. RBC is thus a near-ideal system for experimental investigations of patterns, as well as being an excellent model system for testing theoretical and numerical approaches to the study of the dynamics of nonequilibrium, nonlinear systems.

RBC can be characterized using two dimensionless quantities which depend on the fluid properties: the Rayleigh number R, and the Prandtl number σ. The convection pattern also depends on the geometry of the experimental cell, which can be partly quantified by a third dimensionless parameter. This is the aspect ratio Γ, defined by $\Gamma \equiv r/d$, where r is a lateral size of the cell and d the thickness of the fluid layer.

The Rayleigh number is defined as

$$R = g\alpha d^3 \Delta T/\nu\kappa, \qquad (1)$$

where g is the acceleration due to gravity, d the thickness of the fluid layer, and ΔT the temperature difference across it. The relevant fluid properties are the thermal expansion coefficient α, the kinematic viscosity ν, and the thermal diffusivity κ. R can be thought of as the ratio of the gravitational potential energy to be gained by reversing the unstable fluid stratification set up by the thermal gradient, to the energy cost associated with this reversal due to viscous dissipation and thermal diffusion. Convection begins when R reaches a critical value R_c, corresponding to a critical temperature difference ΔT_c. For an infinite fluid layer bounded by rigid, perfectly conducting plates above and below, $R_c = 1708$. It is experimentally convenient to arrange for ΔT_c to be on the order of a few degrees Celsius, which, for typical fluid properties, implies cell thicknesses on the order of millimeters.

In most convection experiments, the heat input to the bottom of the convection cell, and so ΔT, is varied. Thus R can be thought of as the experimental control parameter. It is convenient to define a reduced Rayleigh number by

$$\epsilon \equiv (R - R_c)/R_c \approx \tilde\epsilon \qquad (2)$$

where

$$\tilde\epsilon = (\Delta T - \Delta T_c)/\Delta T_c . \qquad (3)$$

The onset of convection occurs at $\epsilon = \tilde\epsilon = 0$.

If ΔT_c is small enough, the relevant properties of the fluid change very little over the height of the fluid layer. In this case, the Oberbeck-Boussinesq approximation [6,48,49] can be made in the equations of motion. This approximation amounts to assuming the fluid properties to be constant, except in the buoyancy term of the Navier-Stokes equations, where a variation in the density is needed to drive the convective flow. Stability analysis of the solutions to the equations of motion in this

situation predicts that, at onset, convection will appear via a continuous transition (a supercritical bifurcation) from the uniform base sate to a pattern of infinitely long, straight convection rolls [47]. In this case, the steady-state flow velocity will increase smoothly from zero as ΔT is increased beyond ΔT_c. Experiments with small values of ΔT_c agree with this prediction when they are not unduly influenced by sidewall-forcing effects [12,35,50,51]. A typical shadowgraph image of the pattern close to onset in a large cell is shown in Fig. 2. Here black represents warm, upflowing fluid, and white corresponds to colder downflow. For an Oberbeck-Boussinesq fluid, the approximation in Eq. 2 becomes an equality.
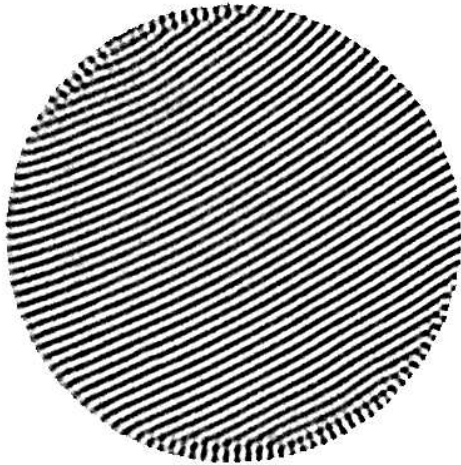

FIG. 2. A shadowgraph image of a pattern consisting of straight-roll convection in compressed CO_2 under Boussinesq conditions. Here $\Gamma = 41$ and $\epsilon = 0.04$. After Ref. [35].
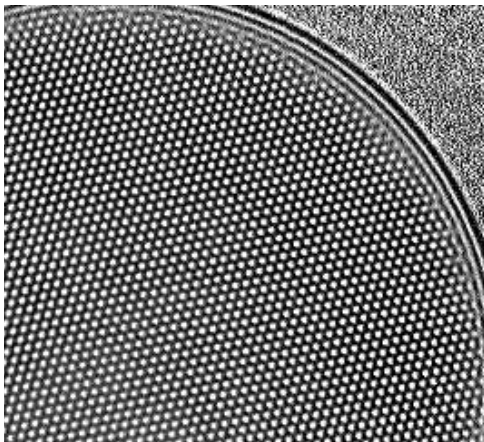

FIG. 3. A shadowgraph image of a hexagonal pattern near the onset of convection in compressed CO_2 gas under non-Boussinesq conditions. Only part of a cell with $\Gamma = 86$ is shown. Here $\epsilon = 0.06$. The concentric rolls near the edge of the circular cell are caused by sidewall forcing. After Ref. [31].

If ΔT_c is large, however, the variation of the properties across the fluid layer must be taken into account. In this non-Oberbeck-Boussinesq case, the onset of convection occurs at a discontinuous transition (a transcritical bifurcation), and the convective flow initially forms a pattern of hexagonal cells [52–56]. A typical shadowgraph image for this case is shown in Fig. 3.

The second important dimensionless parameter is the Prandtl number

$$\sigma = \nu/\kappa, \qquad (4)$$

It indicates the relative importance of inertial terms in the Navier-Stokes equations. This in turn affects the nature of the instabilities to which straight convection rolls are subject above the convective onset [21,22,24]. For gases, σ is typically in the range from 0.7 to 1. For comparison, most other fluids have much higher Prandtl numbers: water at convenient experimental temperatures has σ in the range from 2.5 to 10, and silicone oils can have values of σ in the thousands, depending on their viscosity. The Prandtl number for liquid helium is also of order 1 [57–60], while liquid metals have σ around 10^{-2} [61], but in both of these cases flow visualization is very difficult [61]. The low Prandtl number of gases has a large effect on the behavior of the roll pattern. At low σ, large-scale flows (extending over length scales much larger than a roll wavelength) can be generated by roll curvature. These flows couple back to the rolls, which in turn are then more susceptible to bending, compression, and stretching under the influence of this flow [12,28,29,62–64]. One result of this is that the stability diagram for straight rolls in a gas with $\sigma = 0.7$ is quite different from that for fluids with higher σ. [21,22,24] Another manifestation is the strong tendency to form patterns containing curved rolls and wall foci when ϵ is increased, as shown in Fig. 4. Often this leads to time dependence of the pattern for ϵ as small as 0.1. [28,38,41,58]

FIG. 4. An example of the curved rolls which appear in the Boussinesq case in a cell with $\Gamma = 41$ and for $\sigma \simeq 1$ when ϵ is increased, in this case to 0.34. After Ref. [35].

The time scale for the convective flows is determined by the vertical thermal diffusion time $t_v = d^2/\kappa$. If one considers the pattern to be described by a (spatially varying) amplitude and phase (corresponding, say, to the amplitude and phase of the vertical flow velocity in the center of the layer) [1,18,65–68], then changes in the amplitude of the pattern typically occur over time scales of order t_v/ϵ. For gases t_v is of order a second, whereas for liquids it is more likely to be a minute or so. In all cases, amplitude adjustments are relatively rapid even just above onset. On the other hand, changes in the pattern's phase typically occur diffusively in the horizontal plane, and thus require much longer times, at least of order the horizontal thermal diffusion time $t_h = r^2/\kappa = \Gamma^2 t_v$, and often much longer [69,70]. Thus transients in the convection patterns for samples of large Γ can be extremely slow. In experiments with comparable Γ, they typically are two orders of magnitude faster for gases than for most liquids. Equivalently, on a given time scale, one can study patterns in much larger systems using a gas.

The aspect ratio of the fluid layer not only defines the time scale for phase variations, it also characterizes the extent to which the pattern can show nontrivial spatial behavior. In a small-aspect-ratio cell, the possible dynamics of the pattern are severely constrained, and the effects of the sidewalls can dominate the formation and subsequent behavior of the pattern. Any complexity in the pattern's behavior will be restricted to the time domain if the system is small enough, with the pattern's spatial structure remaining fairly simple [1,71,72]. On the other hand, in a fluid layer with a large aspect ratio, there are many spatial degrees of freedom available to the pattern, and complex spatial and spatiotemporal behavior becomes possible [1,34,57].

Gases have the advantage that one can vary the experimental conditions over a wide range simply by changing the operating pressure P and the mean operating temperature T. This is particularly true for gases near the liquid-vapor critical point, where the fluid properties vary rapidly with temperature [58,73,74]; however, it is noteworthy that σ becomes large as the critical point is approached. Away from the critical point, the fluid properties are not as strongly dependent on T and P, and the primary effect of varying the operating conditions is to vary the density. Both ν (which is equal to η/ρ where η is the shear viscosity and ρ the density) and κ (equal to $\lambda/\rho C_P$, where λ is the thermal conductivity and C_P the specific heat at constant pressure) depend explicitly on density (η and λ are only weakly dependent upon ρ). Thus ΔT_c is approximately proportional to $1/\rho^2$ for a fixed layer thickness d. Equivalently, for a given value of ΔT_c, the required layer thickness is proportional to $\rho^{-2/3}$. On the other hand, σ is roughly independent of ρ. For example, at a temperature of 300 K and a pressure of 1 bar, CO_2 gas has $\sigma = 0.72$, and a critical temperature difference of 5 K requires a layer thickness of 10 mm. At the same temperature and a pressure of 30 bar, $\sigma = 0.95$ and the corresponding layer thickness would be 0.69 mm.

We now consider some constraints on the design of an experimental cell for the study of patterns in RBC in general, and in compressed gases in particular. For the investigation of the behavior of convection patterns very close to onset, i.e., for small ϵ, it is important that ϵ be spatially uniform. This in turn requires that ΔT, and more importantly — because it enters the Rayleigh number to the third power — that the fluid layer thickness d, be uniform over the experimental cell.

Nonuniformities in ΔT can be caused by nonuniform input of heat at the bottom of the cell, nonuniform removal of heat at the cell top or through the sidewalls, or by the different thermal properties of the fluid and the sidewalls. The last of these can cause so-called sidewall forcing, by which horizontal thermal gradients near the walls imprint the geometry of the walls on the pattern which appears at onset [10,12,31,35,75,76]. An example can be seen in Fig. 3, where the hexagonal pattern is surrounded by two or three roll pairs. With negligible sidewall forcing, the convection rolls tend to align perpendicular to the walls as seen in Figs. 2 and 4 where forcing was very weak. Thermal gradients can be minimized by using top and bottom plates with thermal conductivities very much larger than that of the convecting fluid. Sidewall forcing can be reduced further by using sidewall materials with thermal properties matched to those of the fluid [77–80], or through the use of sidewalls specially designed to ensure a buffer region of non-convecting fluid between the bulk of the sidewall material and the sample [29,35,78,79].

Uniformity of the fluid-layer thickness requires the use of rigid top and bottom plates which will not bend or sag. In particular, any pressure differential across the plates, such as might arise when using a compressed gas, will cause them to bend to some degree, with the maximum deflection at the center of the plate increasing as the fourth power of the plate radius [81]. Thus this constraint rapidly becomes more stringent, the larger the lateral size of the cell. The plates must also be accurately flat, and their parallelism should be adjustable when the convection cell is assembled and under pressure.

As in any RBC experiment, it is necessary to ensure that the temperature of the top plate of the convection cell and the heat input to the bottom plate (or the bottom-plate temperature) are well regulated, so that the Rayleigh number is accurately controlled. Since ΔT_c depends rather sensitively on the density for gases, the gas pressure must also be precisely controlled.

Finally, for flow visualization measurements, the RBC cell must be optically accessible. For shadowgraph experiments, this normally means that the top plate of the cell must be transparent, and the bottom plate highly reflecting.

III. REVIEW OF PREVIOUS EXPERIMENTS ON GAS CONVECTION

Flow patterns in thermally-driven convection have been studied for well over a century. In this section, we briefly review some of this previous work. Over the last thirty years or so there has been a very large number of experimental investigations of RBC, and it is not the aim of this paper to review them all. We therefore restrict our discussion of the more recent work to experiments concerned with the onset of convection in gases, and with the formation and behaviour of convective flow patterns in gases at relatively low Rayleigh numbers. In particular, no discussion of Rayleigh-Bénard turbulence [82] will be given.

So far as we know, pattern formation due to convection in fluids was first described in 1855 by Weber [83], who reported that a flow pattern consisting of an array of polygonal cells developed in a droplet of an alcohol-water solution containing a tracer, sitting in ambient air. In 1882 Thompson [84] observed a similar hexagonal pattern in soapy water cooled from the open top surface. Thermal convection is usually associated with the name Bénard [85], however, who observed the formation of hexagonal patterns in well-controlled experiments on an open layer of spermaceti heated from below and cooled from above. All of these early studies described what is now known as Bénard-Marangoni convection [86,87], in which the basic instability is not due to the gravitationally unstable density gradient in the fluid, but to surface tension gradients at the free surface.

So far as we could determine, the first experiments on thermal convection in a layer of fluid contained between rigid top and bottom plates, i.e., on Rayleigh-Bénard convection, were conducted using air at atmospheric pressure as the fluid. These experiments were motivated by the technological question of how the insulating properties of layers of air depend on the layer thickness. It was clear that, due to its small thermal conductivity, air would be a very good insulator. The work of Nusselt [88,89] and Gröber [90] showed that convection contributes to the transport of heat, and so leads to an effective thermal conductivity larger than that of still air. Mull and Reiher [91] conducted a thorough investigation of convection in air at atmospheric pressure, including not only horizontal but also inclined and vertical layers. They investigated samples with heights between 1 and 20 cm and aspect ratios from 42 : 12 : 1 to 5 : 3 : 1. They measured the ratio of the heat transport of the convecting air to that due only to conduction, i.e., what is now known as the Nusselt number. These experiments were later analyzed by De Graff and van der Held [92] and compared with their own experimental results. For the case of the vertical layer, Mull and Reiher [91] visualized the flow from the side using chlor-ammonia fumes as flow tracers.

Motivated by an interest in cloud patterns, Walker and co-workers performed a number of experiments on flow patterns at the onset of convection. Experiments were done with an unperturbed fluid layer, as well as with a constant flow of fluid through the experimental cell, or with an imposed shear flow, to simulate atmospheric conditions. Mal and Walker [93] and Philips and Walker [94] investigated convection in air at atmospheric pressures in a cell of aspect ratio 3.3 : 2.5 : 1 and a height of 6 mm. The convective flow was visualized from below through the transparent glass bottom plate using fumes of titanium tetrachloride. In experiments without throughflow they observed a flow pattern of hexagonal cells. When air was the convecting fluid, the flow in the center of the hexagons was downward, while for liquids the flow was upward. Graham [95] continued the investigations, again with and without shear. To generate shear he used a sliding top plate made of glass, with a stationary iron bottom-plate. For the case of a stationary top plate, he again found, using tobacco smoke as a tracer, descending flow in the center of hexagonal convection cells. He suggested that the sign of the change of viscosity with temperature, which is positive for gases and negative for liquids, is responsible for this effect. This is now known to be the correct explanation [52,96], and the hexagonal pattern observed in these experiments [93–95] can be attributed to non-Oberbeck-Boussinesq effects [55]. In the experiments described above the temperatures of the two plates confining the fluid layer were uncontrolled and were not measured.

A large amount of work has been concerned with the onset of convection. In his seminal 1916 theoretical work Lord Rayleigh [97] showed that convection starts at a non-zero critical value ΔT_c of the temperature difference ΔT. However, since Rayleigh used free-slip rather than rigid boundary conditions for the top and bottom boundaries, the numerical value of R which he calculated did not agree with experimental results. This problem was solved by Jeffreys [98] who extended Rayleigh's calculation to non-slip boundary conditions. This theoretical development lead in turn to a number of experiments. Chandra [99] measured the height dependence of the onset of convection in air at atmospheric pressures. His experimental setup had an electrically-heated stainless-steel bottom-plate and a glass top-plate which allowed observation of the fluid flow. The cell was cooled from above by cold water resting above the top plate. The top and bottom temperatures were measured with platinum thermometers, and another platinum thermometer was positioned mid-way between the plates. The flow was visualized with cigarette smoke. These experiments were continued by Dassanayake [100] using CO_2 at atmospheric pressure. Flow patterns consisting of rolls and hexagons were observed. While the measured Rayleigh number for the onset of hexagons agreed with the Rayleigh-Jeffreys theory (we now know that their experiments must have been performed under non-Oberbeck-Boussinesq conditions), the onset of rolls occurred at a lower value of R than predicted. This dis-

crepancy was later attributed to a rapidly changing non-linear temperature profile resulting from the introduction of the smoke [101].

Another, better-controlled, experiment was caried out at the same time by Schmidt and Saunders [102]. They conducted experiments on both water and air at atmospheric pressure. They used brass bottom and top plates. The bottom plate was electrically heated and the top plate cooled by water circulating through copper tubes soldered into the brass plate. The temperatures were measured with thermocouples embedded in the brass plates. The side walls where made of glass to allow visualization of the convective flow from the side using the shadowgraph technique. This method, discussed in detail below, relies on the temperature dependence of the refractive index of the fluid. Apparently it was first used in a convection experiment by Saunders and Fishenden [103], with water as the convecting fluid. To achieve enough sensitivity in experiments with air, Schmidt and Saunders [102] illuminated the cell with an arc lamp 13 m in front of the cell and observed the shadowgraph on a screen 17 m behind it. Their experiment had a cell spacing of 1 cm and an aspect ratio of $22 : 22 : 1$. Noticeable in their design was the fact that their top and bottom plates were flat to 10 μm, and that the parallelism of the plates was adjusted by levelling the top plate independent of the bottom plate using three screws. A similar technique was used in our own experiments, described below. Their experimental results [102] agreed with Jeffreys' prediction [98] and the early onset described by Chandra [99] was not observed. They also showed that for gases, the pattern becomes time dependent at much smaller ϵ than for water, a phenomenon which we would now attribute to the difference in the Prandtl numbers. Another experiment on convection in air with a superimposed through flow was conducted by Bénard and Avsec [104]. Again, as in the experiment by Chandra [99], the convection pattern was visualized with smoke.

The first experiment to combine heat-transport measurements and flow visualization apparently was conducted by De Graaf and Van der Held using air at atmospheric pressure [92]. They investigated both horizontal and inclined convection layers. The convection cells consisted of two brass plates of size $43 \times 43 \times 0.35$ cm^3, separated by glass spacers of heights 6.9, 12.6, and 22.9 mm. The top plate was water-cooled and the bottom plate heated by an electric heater. The temperatures were measured with thermocouples. The heat transfer was calculated from the change in temperature of the cooling water while it was in contact with the top plate, and its flow rate. The convective flow was visualized from the side using shadowgraphy, with an optical arrangement slightly different from that used by Schmidt and Saunders [102], and from above by visualization with smoke. For horizontal layers they found good agreement with the earlier investigations described above; however, their results for the onset of time dependence disagreed with the observations of Schmidt and Saunders [102].

The observation of time dependent convection and, at higher driving, turbulent convection motivated a number of experiments on convection in air. Thomas and Townsend [105] used a direct (although intrusive) technique to measure the temperature distribution in a convecting air layer. The bottom plate of the experimental cell consisted of a sandwich of asbestos, duraluminum, asbestos, and duraluminum of size 30 cm by 40 cm. The top plate was made of duraluminum and was temperature regulated with circulating water. The lower aluminum plate was heated and the temperature difference across the bottom plate, measured with thermocouples, gave the heat transport through the cell. The two plates were separated by ground glass spacers with heights 3 cm and 5 cm. Resistance thermometers of edged Wollaston wire 3 mm long were mounted on a movable carriage spanning the whole experimental cell. The carriage could be moved vertically or horizontally using micrometer screws, and the resistance of the Wollaston wire was measured in an ac Wheatstone bridge using phase-sensitive detection.

Willis and Deardorf [106,107] used a similar technique. Their rectangular convection cell had a width of 360 cm and a length of 94 cm, and cell heights of 4 cm and 10 cm were studied. The aluminum bottom and top plates were heated and cooled by circulating water baths. They measured temperatures within the convecting fluid with a platinum resistance thermometer placed in the middle of the experimental cell, which could be pulled through the layer at a speed of 25 cm/s to measure a temperature profile.

The experiments by Thompson and Sogin in 1965 are the first we know of on convection in *compressed* gases. [108] They used cylindrical cells of 13.7 cm diameter and heights of 0.3, 0.6, and 1.9 cm. In contrast to what was done in prior experiments, they measured the critical Rayleigh number by changing the pressure and not the temperature difference. Their very well-designed experimental setup is relatively complicated and is described in detail in Ref. [108]. They measured heat transport using air, argon, and CO_2 at pressures from 0.6 to 6.0 bar, and found the critical Rayleigh number to be 1793 ± 80, which compares well with the theoretical value of 1708.

In 1967 Gille [109] used an interferometric technique to visualize the horizontally-averaged vertical temperature field from the side of the sample. He used cylindrical cells of radial aspect ratios $\Gamma = 6.3$ and 4, with heights of 2 cm and 3.1 cm respectively. Air at atmospheric pressure was the convecting fluid. The cell was placed in one arm of a Michelson interferometer, and the observed shifts of the fringe pattern were used to determine the Nusselt number. His results were in good agreement with Nusselt numbers derived directly from heat-transport measurements.

As part of her investigation of the transition to time-dependent flow, Krishnamurti [110,111] studied convection in a variety of fluids including air. Her experimental apparatus is very well described in Ref [110]. The bottom plate consisted of a low-conductivity methyl methacry-

late layer sandwiched between two high-conductivity aluminum plates, with an electric heater in contact with the bottom aluminum plate. Heat transport was measured with thermocouples located above and below the low-conductivity plate. The top of the system was similar in construction but was cooled by circulating water.

Motivated by the observations of oscillatory behavior in earlier measurements made with local temperature probes [92,102], Willis and Deardorf visualized the convective flow in air from above in 1970 [112]. The top plate of their experimental cell was a square glass plate 80 cm wide, cooled with a circulating water bath. The bottom plate was made from aluminum and painted flat black to improve photographic contrast. The cell height was 2.54 cm, and the cell sidewalls were made of plexiglas. The cell height was maintained uniform by 15 small plastic spacers positioned throughout the cell. Heat was applied to the bottom plate using a thin electric heating pad resting on a second aluminum plate. The convective flow was visualized using an oil smoke composed of atomized particles of dioctyl phthalate with an average diameter of 150 microns. They clearly observed the oscillatory instability later found theoretically in the stability analysis of Clever and Busse [21,22]. The same apparatus [112] was used by Willis, Deardorf and Sommerville [113] to investigate the behaviour of the wavenumber of the convection pattern as a function of the Rayleigh number. In this work, the flow was again visualized with oil smoke. It is interesting to note that the photograph of the convection pattern shown in Figure 3 of Ref. [113] appears to show spiral defects. Spiral defects, and a disordered, time-dependent convection state referred to as spiral-defect chaos have recently been studied by us in compressed CO_2 gas [34,39,41].

In the early 1970's, one of us started to use gaseous (as well as liquid) helium to study RBC at cryogenic temperatures. [57,114] The sample was cylindrical, with a radial aspect ratio $\Gamma = 5.5$. The techniques of low-temperature physics afforded the opportunity of much higher temperature resolution than could be accomplished at the time with room-temperature techniques. The negligible heat capacity of the bottom plate made it possible to study the time dependence of the Nusselt number $\mathcal{N}$, and led to the discovery of non-periodic time dependence (chaos) in this system for Rayleigh numbers larger than twice the critical value. The time dependence of the heat transport also revealed [115] the oscillatory instability found by Willis and Deardorf [112], and gave its onset and frequencies in good agreement with the theoretical calculations [21,22]. Time-averaged Nusselt numbers were determined [57,114] for Rayleigh numbers up to 2.5×10^5 ($150 R_c$). In spite of their high resolution, these experiments did not show any of the transitions in the heat-flux curves which had been reported previously by others [116,117]. The $\Gamma = 5.5$ cell was also used with helium gas to study effects of departures from the Boussinesq approximation on the heat transport [118]. Much of this work at cryogenic temperatures was reviewed by

Behringer [60].

At approximately the same time, helium gas at low temperatures was also used by Threlfall [119], but in a cylindrical container with the rather small aspect ratio $\Gamma = 1.25$. His work concentrated on Nusselt number measurements at very high Rayleigh numbers, up to $R \simeq 2 \times 10^9$. At sufficiently large R he showed that $(\mathcal{N} - 1) \propto \epsilon^{0.28}$. Scaling arguments [120] had suggested that this exponent should be 1/3; but at the present the slightly smaller value is generally accepted [82].

Oertel and Bühler [121,122] used a $\lambda/2$ compensated differential interferometer to visualize convection in gases at atmospheric pressure from the side. With this visualization technique phase objects having optical path differences of from $\lambda/30$ to 100λ can be visualized. Both lines of equal horizontal and vertical density difference can be visualized as interference fringes. This technique was also used in other, similar experiments by Martinet et al. [123,124] and by Zierep and Oertel [125]. All of these interferometric studies suffer from the disadvantage that, since the refractive index of air is not much different from 1, it was necessary to view the convection from the side, and so to integrate over the length of the convective rolls to obtain an optical path length through the convection cell sufficient to show interference fringes. This results in the loss of information about spatial variations along the length of the rolls.

Another series of experiments was conducted by Leith [126–128] in air at atmospheric pressure. The convection cell had dimensions 24 cm by 16 cm by 2 cm. The top and bottom plates were made of paraffin-filled foamed aluminum with embedded tubes used for temperature regulation with a circulating water bath. The convection was visualized from the side through thick plexiglass sidewalls by injecting smoke into the gas. Temperatures were measured with thermocouples located in the top and bottom plates. Four differential thermocouples were installed in the interior of the air layer. Leith used this apparatus to investigate wavenumber selection and dislocation defects in the convection pattern.

Extensive studies of patterns in pressurized argon have been carried out by Croquette, Pocheau, and coworkers [12,28,129,130,30,131–135]. The apparatus consisted of a container holding compressed argon at pressures on the order of 50 bar. The top window, which supported this pressure, was made of a thick single crystal sapphire. The same sapphire also served as the top plate of the convection cell, and was cooled by a circulating water bath. Because of this, bending of the top plate due to the pressure it supported introduced an inhomogeneity in the cell height. However, for the cell height of about 1 mm and the relatively small diameters used, these variations in height were not very important. The bottom plate was a thick copper mirror heated by an electric heater. The sidewalls were formed by a plastic spacer. When used for heat-transport measurements the bottom of the cell was surrounded by a thermal shield in order to minimize heat losses through the side. Their gas layers had ra-

dial aspect ratios Γ up to 22. A shadowgraph technique was used for the visualization of the pattern, taking advantage of the fact that an increase in pressure leads to an increase in the refractive index of the gas, and so to an increased shadowgraph sensitivity. The cell was illuminated with a point light source in the focal spot of a convex lens. Parallel light entered the cell and was reflected back through the lens from the bottom plate. A beam splitter located between the light source and the lens directed the reflected light into a second lens, which imaged the shadowgraph on the focal plane of a camera. This optical setup is very similar to the one used by us, as discussed later in this paper. These experiments have led and are still leading to numerous important results pertaining to pattern formation in Rayleigh Bénard convection, and are reviewed in Refs. [1,12,19,28].

In 1978, Ahlers and Behringer [58,59] took advantage of the fluid properties near the critical point of ^{4}He to study convection in a cell of very small spacing and thus of relatively large aspect ratio $\Gamma = 57$. This work led to the then surprising discovery that RBC in large-Γ cells becomes time dependent near or below $\epsilon = 0.1$, much closer to the onset of convection than had been predicted [21,22] on the basis of the stability analysis of straight rolls. This phenomenon is now understood at least qualitatively on the basis of the beautiful experiments of Croquette, Pocheau, and coworkers [28], as well as from some of our more recent work [35,38,41]. As ϵ increases, there is a growing tendency for rolls to terminate with their axes perpendicular to the sidewall. In a circular container, or near corners in a rectangular one, this leads to strongly curved rolls like those in Fig. 4. For small σ, this curvature induces a large-scale flow which causes the wavenumber in the pattern interior to increase beyond the relevant straight-roll instability, namely the skewed-varicose instability. Generation, climbing, and gliding of defects then leads to time dependence before the average wavenumber of the pattern has crossed a stability boundary.

Recently the opportunities offered by a gas near a critical point were exploited more extensively by Assenheimer and Steinberg [73,74], who conducted an experiment in pressurized SF_6 near the gas-liquid critical point. The convection cell had a design very similar to that described by Croquette et al. [12]. The water-cooled top plate (and pressure window) was a 19 mm thick sapphire with a diameter of 102 mm. The cell bottom plate was a nickel plated copper disk, to which an electric thermofoil heater was attached. The cell sidewall was formed by a mylar spacer 130 μm thick. The very small cell thickness was possible due to the properties of the experimental fluid close to its gas/liquid critical point [136,137]. The experimental volume was coupled via a thin tube to a small "hot" volume [138], the temperature of which was varied to control the pressure of the convecting fluid. This method is also used in our apparatus and will be described in more detail below. The convective planform was visualized from above by shadowgraphy. The great

advantage of performing convection experiments close to the critical point lies in the tunability of the fluid parameters and the opportunity to reach very large aspect ratios. However, only Prandtl numbers significantly greater than one can be reached since σ diverges at the critical point. As before, the main disadvantage of the above design is the cell-height inhomogeneity due to the bending of the top sapphire. In this case, height variations on the order of 1.8 μm over the diameter of the cell lead to a variation of ΔT_c of 4%. These experiments are also producing many interesting new results [73,74].

Very recently a gas convection experiment was performed by Keat [139] as an undergraduate laboratory experiment. The setup was very similar to the one used by Croquette [12]. It was used to reproduce some of the results obtained by Croquette et al [12], and to visualize the onset of low-dimensional chaos via a period-doubling cascade [71,72]. The bottom plate was made of silicon resting on a copper plate that was electrically heated. A polished silicon bottom plate had been used previously by Kolodner [140] in binary-fluid convection. It gives excellent flatness, resistance to distortion over time, and enough reflectivity for shadowgraph flow visualization.

Our own experiments on convection in compressed gases, conducted during the last seven years, are described in the next two Sections.
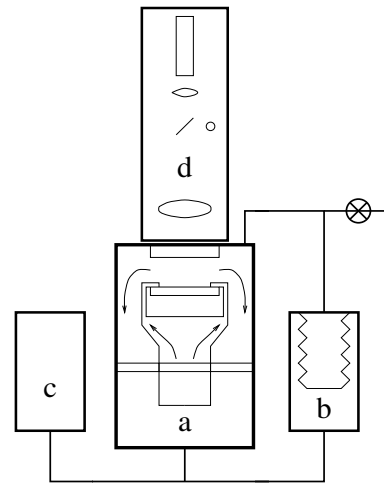

FIG. 5. A schematic diagram of the apparatus, showing the main components. The sample cell is contained in the main pressure vessel (a). A second pressure vessel (b) contains a bellows used to equalize the pressures between the sample gas, in the dry region of the main vessel, and the internal water bath, in the wet region. Another pressure vessel (c) is used as a ballast volume in the control of the pressure. The flow-visualization optics (d) are contained in a tower which is mounted on top of the pressure vessel during experiments. A personal computer is used to control and run the experiment.

IV. APPARATUS

A. Overview

An overview of the apparatus used by us to study RBC in compressed gases is provided by Fig. 5. The convection-cell assembly is mounted inside a pressure vessel (a). The space within this vessel is divided into two regions, which we refer to as "wet" and "dry." The wet region contains a pump which circulates temperature-controlled water over the top plate of the cell, while the dry region contains the experimental gas. Heat is applied to the bottom plate of the cell, which is dry, by a film heater. Water flowing through a cooling jacket on the outside of the vessel (not shown) removes heat from the system. Feedthroughs at the bottom of the vessel provide access for electronics and gas lines. A bellows, either in an external pressure vessel (b) as shown in Fig. 5 or inside the main vessel, is used to pressurize the wet region when the dry region is being filled with the gas. Another external pressure vessel (c) serves as a ballast volume for control of the gas pressure. The top plate of the cell is transparent, and a thick sapphire window on the top of the pressure vessel supports the pressure. In this design there is no significant pressure difference supported by the cell top or bottom, thus minimizing any distortion of the cell geometry. The windows allow visualization of the convective flow using the shadowgraph technique. The shadowgraph optics are mounted in a tower (d) which sits on top of the pressure vessel. Prior to a run, this tower is replaced by interferometers used to align and measure the thickness of the cell. Below we describe these components in detail.
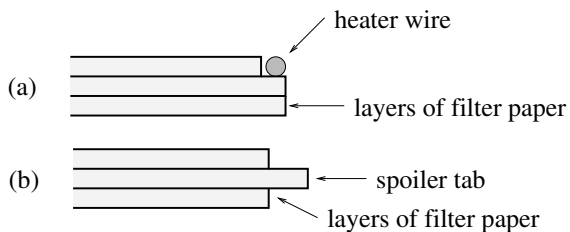

FIG. 6. Details of the sidewall geometries described in the text. (a) Detail showing the heater wire positioned at the edge of the paper sidewall, to allow for intentional application of sidewall forcing. (b) A "spoiler tab" used to reduce sidewall forcing. The thinner layers of gas above and below the tab remain below the onset of convection, and have thermal properties matched to those of the convecting gas in the bulk of the cell.

B. Convection Cell

There are several demands on the cell design, as outlined above. The top and bottom plates must be made of materials with high thermal conductivities, relative to the experimental fluid, to avoid lateral thermal gradients, particularly near the edges of the cell. To minimize sidewall forcing, the cell sidewalls ideally should have a thermal diffusivity and conductivity as close as practical to that of the fluid. To allow shadowgraph visualization of the flow pattern, the top plate must be transparent, and the bottom plate must be highly reflecting. The top plate separates the wet and dry regions of the pressure vessel, and since we want the cell thickness to be extremely uniform, it must be sufficiently thick that it does not bend appreciably under any pressure difference between the two regions. Finally, the thickness of the cell, and more importantly, its uniformity, must be adjustable when the system is under pressure so that nonuniformities which develop during pressurization can be removed.

Since the thermal conductivities of gases are very low (on the order of 0.02 W/Km) compared to most solids, the first of the above criteria is easily satisfied. For the top plate we used sapphire windows ($\lambda = 35$ W/Km), 0.95 cm thick and 10.2 cm in diameter, polished flat to 0.1 μm over the central 80 % of the window area [141]. Thinner sapphire windows cannot be polished as flat and tend to bend when they are mounted in the apparatus. We used various materials for the bottom plate, including sapphire with an evaporated layer of aluminum, and various metals. Most recently we used aluminum ($\lambda = 240$ W/Km), 0.95 cm thick and 10.2 cm in diameter, diamond machined to a mirror finish and a flatness of 1 μm across the diameter of the plate [142].

We used several different types of sidewalls. The whole dry region of the apparatus, including the cell assembly, is flooded with the gas which enters the cell through the sidewall. Thus the sidewall must not provide a leak-tight seal. However, it does have to isolate the flow in the gas sample from the gas outside of the cell, since otherwise any flows outside might influence the convection within the cell. If the top and bottom plates had infinite conductivity, a mismatch in the conductivity of the gas and the sidewall would not matter. In practice, the bottom plate had a very high, effectively infinite conductivity, but the conductivity of the top sapphire plate was large but finite. Consequently, the heat current passing through the wall, which was larger than that passing through the gas, induced a larger vertical temperature gradient in the sapphire than the current through the gas. This created a small but significant *horizontal* temperature variation near the top of the sample and the sidewall. This effect would vanish only if the conductivity of the sample and the sidewall were equal, a situation difficult to achieve with gas convection. We considered various plastics for sidewall material, but they could not be used in experiments with CO_2 because they tended to absorb the gas and swell over time. In our early experiments [31], we used sidewalls made from a machinable ceramic, Macor ($\lambda = 1.26$ W/Km) [143]. More recently [34,35,38,39,41,42], we used walls made from multiple layers of filter paper, cut to the desired shape. The thermal conductivity of the paper is only about a fac-

tor of 10 larger than that of the gas, whereas that of Macor is larger by a factor of 50 or so. As a result, the paper sidewalls cause less sidewall forcing than Macor, and so the cell geometry has a lesser effect on the convection pattern. In addition, the compliance of the paper distributed the contact stresses which would cause distortions in plates sandwiching a rigid spacer, and allowed some adjustment of the thickness. When desired, a thin heater wire could be placed around the edge of the paper sidewall, as shown in Fig. 6(a), to allow the application of intentional thermal forcing at the cell edge. This made it possible to initialize an experiment with a pattern consisting of rolls parallel to the walls. In some experiments [35], cell sidewalls with "spoiler tabs" [29,78,79] were used, as shown in Fig. 6(b). In this sidewall geometry, a thin tab extends into the fluid from the main sidewall. The layers of gas above and below the tab are sufficiently thin that they are below the onset of convection even when the fluid in the cell interior is well above onset. Thus the convecting fluid to a large extent feels the thermal properties of these quiescent gas layers, rather than those of a solid sidewall. In other experiments the sidewall forcing was varied [35,38], and its effect on the convection pattern studied, by adjusting the thermal contact between the sidewalls and the top and bottom plates. This was done by adjusting screws which changed the force with which the paper sidewalls were pressed between the two plates.

In order to gain some insight into the thermal forcing associated with various sidewall options, temperature fields near the walls in the absence of convection were calculated [144]. The calculation was done by assuming constant-temperature boundary conditions at the top of the bottom plate (bottom of the fluid) and at the top of the sapphire. This is consistent with an effectively infinite bottom-plate conductivity and a large but finite conductivity of the sapphire. Shown in Fig. 7(a) is the temperature field in the fluid near a Macor sidewall. (Note that the Macor sidewall actually used in Ref. [31] had a small step, unlike the sidewall modeled in Fig. 7(a). This step increased the effects of sidewall forcing in the experiments reported in Ref. [31].) The contour lines shown in the figure correspond to constant deviations of the temperature from the vertical temperature gradient which would exist in the laterally infinite system without a sidewall. The numbers labeling the lines are the deviation, in units of 0.1% of the total imposed temperature difference. As can be seen, at the top of the fluid there is a lateral temperature variation of about 1% over a distance of about $2d$ near the wall. In Fig. 7(b), the Macor is replaced by paper. The temperature variation at the top of the fluid is reduced to about 0.3 % but extends over about the same lateral range. In Fig. 7(c), there is a paper sidewall with a 0.001 cm gap containing the gas between the paper and the sapphire. This case was studied since it may be expected to represent approximately the case of a paper sidewall which is not compressed very firmly between the top and bottom plate.

The results show a substantially enhanced temperature distortion due to the gas layer. The reason for this is that the top of the sidewall reaches a relatively high temperature because the wall conductivity is substantially larger than that of the gas above it, leaving a steep thermal gradient across the relatively thin gas layer. The horizontal temperature variation in the fluid is as large as 8%. In an attempt to reduce its lateral range, a spoiler tab was added to the sidewall of Fig. 7(b). The resulting temperature field is shown in Fig. 7(d). The temperature distortions near the gaps above and below the tab are as big as in 7(c), but since the tab physically prevents convection in the region where the deviations are large, the deviations do not matter. The end of the tab defines the region over which the fluid can convect, and it is the distortion of the temperature field generated to the right of the tab that is important. The deviation near the tab is around ±11%, but this field is dipole-like and decreases rapidly away from the tab, reaching below 0.1% just $1d$ into the cell.

The relatively strong forcing of the Macor sidewall of Fig.7(a) yielded patterns like those in Fig. 3, where two or three roll pairs parallel to the sidewall surrounded the pattern in the sample interior. In Fig. 8, we show the patterns which evolved when ΔT was increased quasi-statically with walls which corresponded roughly to cases (c) and (d) in Fig. 7. Both walls produced a pattern of concentric rolls when ΔT was increased quasi-statically in very small steps. However, in the case of the spoiler tabs these rolls were surrounded by a ring of cross rolls with their axes perpendicular to the wall.

In an attempt to further minimize thermal sidewall forcing, we also used a sidewall with a cross section which had the shape of the letter **H**. The vertical pieces were each only 0.1 mm thick and we expected them to have only a small influence on the thermal gradients. With this design, convection appeared in the form of 3-5 circular rings next to the sidewall before the rest of the cell convected in the form of straight rolls.

Although it was difficult to find a wall design that eliminated forcing, it was possible to create a pattern of straight rolls by first increasing ΔT to a large value where a highly disordered flow pattern evolved, and by then decreasing it again to the vicinity of the threshold. With patience, this created patterns like the one shown in Fig. 2. Once formed, the straight rolls were stable (in the Boussinesq case) even in the vicinity of the onset, unless the sidewall forcing was quite strong. As can be seen, there are no rolls parallel to the wall in Fig. 2 because the sidewall forcing was weak enough.
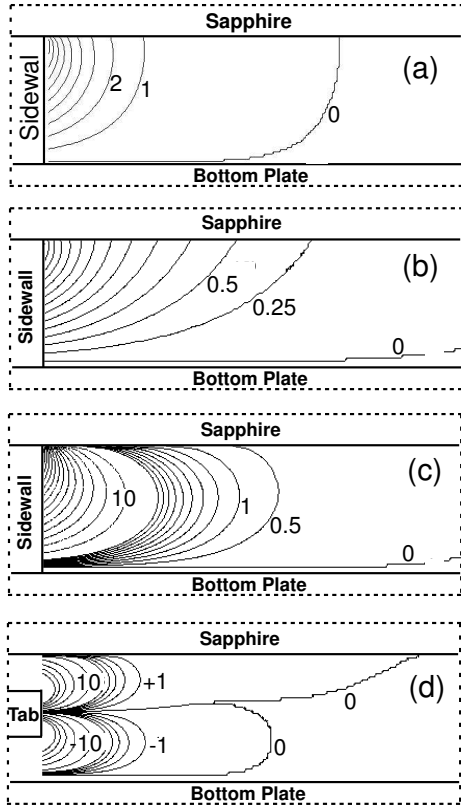
FIG. 7. Deviations from an ideal constant vertical temperature gradient near the sidewall. The contour lines show deviations from the ideal profile and are labeled in units of 0.1%. Only a small part of the sample, corresponding to a horizontal distance of about $3.4d$ from the wall, is shown. The lengths in each figure are scaled by d. In (a) there is a Macor sidewall confining the sample, and $d = 0.052$ cm. In (b), the Macor sidewall was replaced by a paper sidewall of height $d = 0.105$ cm without any gaps between the sidewall and the top and bottom plates. In (c) there is a gas layer of thickness 0.001 cm above the paper wall of (b). This case is more likely to be representative of the real experiment than case (b). In (d), a spoiler tab is added to case (b). In part after Ref. [35].
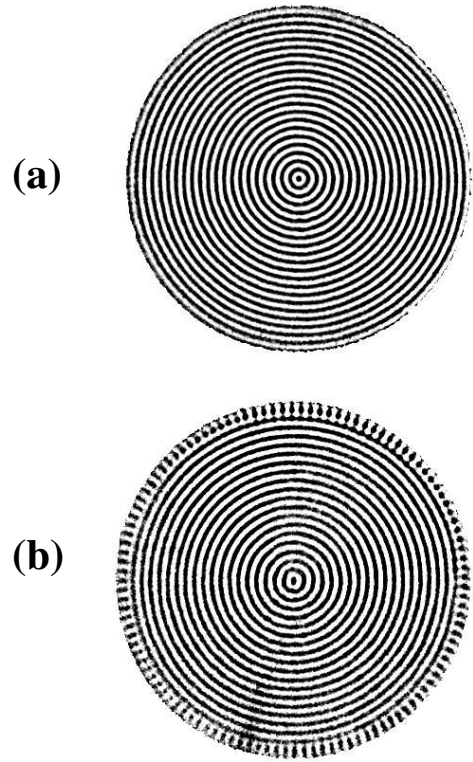
FIG. 8. The concentric-roll patterns which formed in the case of two of the sidewalls shown in Fig. 7 when ΔT was increased quasistatically from below to above ΔT_c. (a) corresponds to Fig. 7(c), and (b) to Fig. 7(d). After Ref. [35].

The cell is assembled in such a way that it is possible to make fine adjustments to the parallelism of the top and bottom plates both before and after it is pressurized. The cell assembly is illustrated in Fig. 9. The topmost component is a stainless-steel flow distributor (e and f), which directs circulating temperature-controlled water onto the sapphire top plate (c). The water emerges both from jets (f) and between the tabs at the periphery of the sapphire. This flow distributor is initially attached to the top plate at three points by small dabs of silicone cement. This simple three-point mounting of the sapphire plate minimizes mechanical stresses on the plate. The flow distributor has a series of tabs around its inner circumference, which are pressed against the circumference of the sapphire top plate by a clamping ring (g). Below the flow distributor is a stainless-steel ring (h) which seals around the circumference of the sapphire with an O-ring. Below this ring is another stainless-steel piece (m) which holds the bottom-plate assembly, and this piece is in turn sealed against a stainless-steel can (n) which surrounds the entire lower part of the cell assembly. Distortions of the top plate when it is held in this assembly amount to less than 0.3 μm across its diameter.
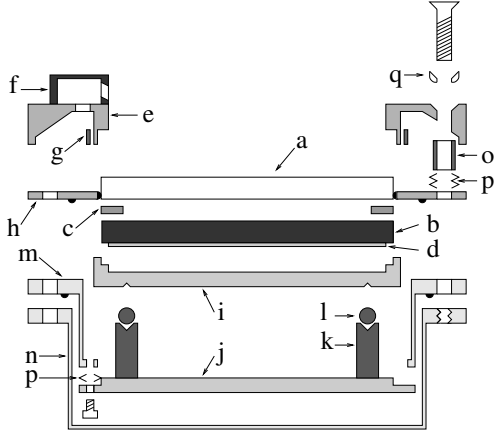
FIG. 9. Assembly of the experimental convection cell. See text for a detailed description. a) sapphire top plate; b) cell bottom plate; c) sidewall; d) bottom-plate heater; e) flow distributor; f) jet; g) clamping ring; h) top-plate holding-ring; i) hardened steel plate; j) bottom support plate; k) legs (passive or with piezo-electric transducers); l) ceramic balls; m) cell-bottom-assembly holder; n) can; o) sleeve; p) spring washers; q) ball washer.

The tilt of the flow distributor and top-plate assembly could be adjusted to make the top and bottom plates parallel. This was done using three screws which connect the flow distributor to the can via Belleville disc spring washers (p). These screws were positioned with ball washers (q) (machined from steel balls) to minimize mechanical stresses. In one version of the apparatus, these three screws were made accessible to atmospheric pressure by rods which passed through Ultra-torr O-ring fittings in the top flange of the pressure vessel. They could thus be used for alignment of the cell even when the experiment was under pressure. In another version, these screws were only used for coarse alignment before the system was pressurized, and a system of three piezo-electric transducers, described below, was used for fine adjustments while under pressure.

The bottom plate of the cell rests on three small steps machined in the edge of a hardened steel plate (i). This plate is kinematically mounted on three legs (k) via three ceramic balls (l). These balls served to cut the thermal leak between the hardened steel plate (i), which was generally at the same temperature as the bottom plate (b), and the lower part of the cell assembly (m and j), which was near the top-plate temperature. Three springs under tension (not shown) pulled the steel plate down onto the legs. The legs were in turn mounted on a rigid steel supporting plate. This plate was connected to the rest of the cell assembly by three small screws with spring washers (p), centered with ball washers (not shown), which could also be used for coarse adjustments of the relative align-

ment of the top and bottom plates. The entire gas-filled volume in the lower part of the can was filled with open-pore foam material, or with pieces of aluminized mylar super-insulation, to insulate the bottom plate and prevent convection.

In one version of the experiment, the three passive legs holding up the hardened steel plate and the bottom plate were replaced by three legs containing piezo-electric transducers. We used unpackaged multi-layer low-voltage piezo-electric stacks [145], 12 mm long, which had a maximum extension of 12 μm for an applied voltage of 120 V, and a shorter range of negative extension for negative applied voltages. Each stack was built into a stainless-steel leg and actuated a small steel cup which held the ceramic bearing. Springs served to keep the stacks under tension, which is the recommended mode of operation. The use of unpackaged stacks, which are solid pieces of multilayer ceramic painted with an epoxy insulator, avoided the use of plastic parts which were found to deteriorate under prolonged exposure to the high-pressure CO_2 used as the experimental fluid. The drive voltage for the piezo-electric stacks was taken from a precision 120 V DC supply via three voltage dividers. The drive circuitry incorporated capacitors and an interlock system which maintained the voltage in the event of a power failure. The power supply and some pressure-control electronics were mounted in a box which was temperature controlled to $\pm 0.1°$C to improve long-term stability. The stability of the cell geometry was not limited by that of the piezo-electric legs. The piezo-electric legs worked about as well as the top-plate screws for making the plates parallel, with the latter giving more range of movement while the former allowed more control over a shorter range. In both cases, it was possible to use interferometric methods, described in Section D below, to prepare cells which were parallel to within the limits imposed by the flatness of the top and bottom plates, that is, to about ± 0.3 μm across their diameter. In a cell with thickness $d = 0.5$ mm, this corresponds to a uniformity in d of better than 0.1 %.

During a run, the top plate of the cell was maintained at a constant temperature by temperature-regulated water which circulated across it. A circular thin-film heater with diameter equal to that of the bottom plate [146] was glued onto the bottom plate; the plastic in which the heater wire was embedded was perforated with many pinholes to prevent its coming unglued when the system was depressurized. The temperature of the bottom plate was measured using calibrated thermistors [147] embedded deeply in small holes in the bottom plate. Wires making connections to the bottom-plate heater, thermistors, and piezo-electric elements passed through a thin-walled $\frac{1}{4}$in o.d. stainless-steel tube to the bottom of the pressure vessel, where they were connected to external instrumentation via high-pressure feedthroughs.

C. Pressure Vessel

The cell assembly described above was contained in the stainless-steel pressure-vessel shown in Figs. 5 and 10. The circulating water used for temperature control was pressurized along with the sample gas, to minimize the pressure difference across, and hence the distortion of, the cell top- and bottom-plates. Thus the circulating pump is housed inside the vessel, along with several pieces which direct the flow, or are used for controlling the temperature of the circulating water. Most components inside the vessel which were in contact with the pressurized gas were machined from stainless steel or aluminum. Plastics in the gas space had to be avoided because of problems due to the gas diffusing into or through them.
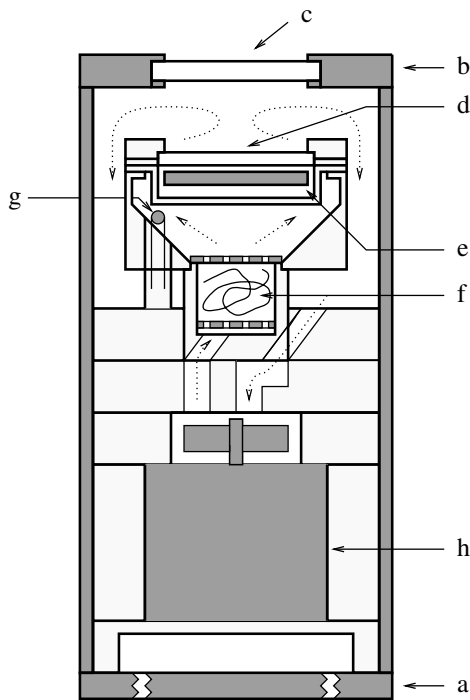

FIG. 10. Schematic diagram of the main pressure vessel. a) bottom flange; b) top flange; c) top window; d) cell top plate; e) cell bottom plate; f) bath heater; g) bath thermistor; h) circulating pump. The dotted lines indicate the flow of the circulating temperature-controlled water. See text for a detailed description.

The vessel was designed to be used up to 100 bar, with a substantial safety factor [81]. It was machined from stainless-steel pipe, and had an inside diameter of 15.9 cm and a wall thickness of 0.95 cm. Stainless-steel top- and bottom-flanges were attached and O-ring sealed to the body of the vessel with grade 8 hardened-steel bolts. The bottom flange was 2.2 cm thick. It contained several holes with 1/4 in female pipe threads into which a valve and several high-pressure feed-throughs [148] for electrical connections and for stainless-steel gas-handling tubes were screwed. The top flange was 2.5 cm thick, and held

a 1.9 cm thick by 10.2 cm diameter window, made of a single-crystal sapphire. Glass, or even fused silica, of similar thickness was considered too weak to safely support the pressure difference because of surface and internal defects.

At the bottom inside the vessel, an aluminum plate with a large recess machined into it provided a place for making electrical connections to the wires passing through the bottom flange. Above it was a large aluminum piece which held the pump. The pump was a modified magnetically-driven aquarium pump [149]. Its motor was removed from the original plastic housing and potted with Stycast 2850FT epoxy [150] into a stainless-steel box. A glass-sealed electrical feedthrough on the stainless-steel pump-box was used to connect ac power to the pump motor. An O-ring at the top of the pump box was one of several which separated the wet and dry regions. Above the pump was a stainless-steel flow-distributor plate with channels milled into it to direct the flow of water out of and back into the pump.

Roughly in the center of the pressure vessel, above the flow-distributor plate, was the main stainless-steel platform. An O-ring around its circumference formed a seal to the wall of the vessel, again to isolate the dry from the wet region. In the center of this platform was a delrin chamber, bounded at its top and bottom by two thin stainless-steel disks with many holes drilled in them. Between these disks was the bath heater, which consisted of roughly 18 m of #30 insulated single-strand copper wire, with a resistance of about 7.5 Ω. Water coming out of the pump passed through this chamber on its way up toward the cell region. After leaving the heater chamber, the water was directed upward around the outside of the stainless-steel can surrounding the cell assembly by a delrin flow separator. On its way up, the water flowed over four 100 kΩ thermistors [147] which were held in stainless-steel turrets attached at 90° intervals around the main platform.

The thermistors and the bath heater were used to control the temperature of the circulating water using a personal computer (PC). The four thermistors which measure the temperature of the water just above the heater chamber were arranged in a series-parallel network, so that the total resistance of the network represents an average of the temperature around the flow. The resistance of the thermistor network was read with a $6\frac{1}{2}$ digit ohm-meter, and transmitted to the PC over an IEEE-488 bus. A program monitored the resistance and compared it to a desired set point, then used a proportional-integral-differential control algorithm to adjust the bath-heater voltage via a digital-to-analog converter. This system provided short-term temperature stability of ± 0.2 mK. Long-term stability is limited by room-temperature variations which cause drifts in the calibration of the measuring instruments, and is estimated to be about ± 1 mK.

The temperature-controlled water is directed onto the cell top-plate by the flow distributor. Water is directed down onto the top plate from above by jets mounted on

the flow distributor, and across the surface of the plate through notches milled in the bottom of the flow distributor. Heat transported through the convection cell during an experiment is efficiently swept away by the flow of water. Temperature gradients across the cell top-plate due to its finite thermal conductivity, and due to the presence of the sidewalls, are estimated to be typically on the order of 0.3% at the onset of convection.

After passing over the top plate, the water returns to the pump. It flows down around the outside of the delrin flow separator, thus providing thermal insulation between the pressure-vessel wall and the upflowing water inside the separator. The complete flow path of the water is shown in Figs. 5 and 10.

Heat is removed from the pressure vessel by an external cooling jacket positioned roughly at the height of the pump motor (not shown in the figures). Water was circulated through this jacket by a temperature-controlled circulating bath. In one version of the apparatus this heat removal was not provided, and cooling was only to the ambient air at approximately 20°C. In that case, the bath could not be operated below about 32 °C.

We also found it necessary to control the pressure of the sample gas. Room-temperature variations, and the slow diffusion of the pressurized gas through the butyl-rubber O-rings or into plastic pieces, caused pressure variations over the course of a run (i.e., over several weeks) which in turn caused drifts in ΔT_c. To eliminate these drifts, the pressure was controlled using a temperature-regulated external ballast volume [138], connected to the main pressure vessel, as shown in Fig. 5. The gas pressure was measured using a commercial strain-gauge pressure transducer [151], and a voltage was applied to a heater in the ballast volume to change its temperature such that the pressure remained constant. The variation in pressure using this system was ±0.01% (0.001% in a version using a home-made pressure transducer [152]), and ΔT_c varied by less than 0.02% with this level of pressure control.

A second external volume contained a bellows which was used to pressurize the wet region of the main pressure vessel (in one version of the apparatus, the bellows is in the main pressure vessel, and forms part of the can surrounding the cell assembly). One side of the bellows was in contact with the wet region, the other with the dry, as shown in Fig. 5. To prevent corrosion, welds joining the bellows to a mounting plate were covered with Stycast 2850FT epoxy [150]. The roughly 2 l volume of the water in the wet region decreases by about 0.1%, or about 2 cm^3, when it is pressurized, due to the finite compressibility of the water. This, and the compression of any air remaining in the wet space, is compensated for by the expansion of the bellows. The force required to extend the bellows results in a pressure difference between the wet and dry regions — and so across the sapphire top plate of the cell — of typically 1 psi. This causes the sapphire to bow outward at its center by about 0.1 μm.

D. Cell Alignment and Thickness Measurement

The parallelism of the top and bottom plates was adjusted and the thickness of the cell measured using two different interferometric techniques. Initially, the cell was assembled and mounted on a stand. A helium-neon laser beam, expanded and collimated to illuminate the entire cell, was directed normally into the cell. Light reflected from the bottom surface of the sapphire top-plate and from the mirror surface of the bottom plate was then directed onto a screen by a beam splitter. This arrangement is shown in Fig. 11. The interference fringes observed on the screen are fringes of equal thickness [153]; each fringe corresponds to a change in the optical thickness of the cell of one-half of a wavelength. The cell thickness is made uniform by adjusting the three screws which connect the bottom support plate to the rest of the cell assembly and the three screws which connect the top flow distributor to the assembly. It is straightforward to get the two plates parallel to within a few fringes, i.e., to within about 1 μm.
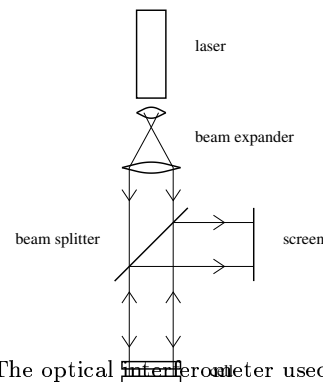

FIG. 11. The optical interferometer used for adjusting the parallelism of the top and bottom plate of the convection cell.

Once this preliminary alignment has been performed, the cell is mounted in the pressure vessel. The pressure vessel is then leveled, using a precision level placed on the sapphire top-plate of the cell, to make the cell accurately horizontal. The upper, wet half of the vessel is then filled with water and the vessel closed. The system is pressurized as described below, the internal water bath temperature-controlled at the desired operating temperature, and the bottom plate brought to a reference temperature just below the onset of convection. Mechanical stresses from mounting the cell, thermal expansion, and the small pressure differential across the cell top-plate all contribute to the misalignment of the cell plates after this procedure, and a further fine adjustment of the cell parallelism *in situ*, at the operating temperatures and pressure, is required. This adjustment is performed using the same procedure as described above, except that the laser, beam splitter, and screen assembly are mounted on top of the pressure vessel rather than on a separate stand. The final alignment was done with the three piezoelectric

15

stacks, or with the three externally accessible screws in the flow distributor described above. Using either procedure, the cell could be restored to within about 0.3 μm of parallel at the reference temperature. The system was sufficiently stable that this alignment persisted for the few weeks' duration of an experimental run. For the largest temperature differences applied across the cell, thermal expansion of the bottom plate caused a change away from parallelism corresponding to a few fringes; parallelism returned without hysteresis when the bottom plate was returned to the reference temperature.
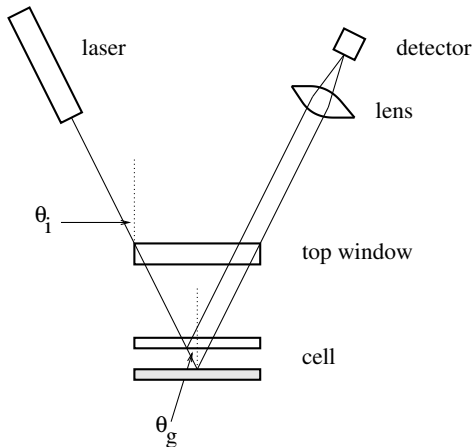
FIG. 12. Schematic drawing of the interferometer used for measuring the cell thickness. See text for a detailed description.

The thickness of the pressurized cell was measured with a second type of interferometer, which was mounted on top of the pressure vessel for this purpose. It is shown schematically in Fig. 12. A helium-neon laser and a large-area photodiode detector assembly [154] independently move on lever arms which pivot about an axis passing through the convection cell. The unexpanded laser beam reflects from the bottom plate of the cell and the bottom of the sapphire top plate at an adjustable angle θ_i. The two reflected beams emerge parallel and very slightly displaced from each other. They are directed onto the photodiode assembly by a beam splitter and focussed onto it by a 2.54 cm focal length, 2.54 cm diameter lens. These beams interfere on the detector to produce fringes of equal inclination [153]. The condition for interference minima is

$$m\lambda = 2n_g d \cos \theta_r \qquad (5)$$

where m is the (integer) fringe order, λ the laser wavelength, n_g the refractive index of the gas in the convection cell, d the cell thickness and θ_r the angle the ray traveling through the cell makes with the normal to the cell plates. The refractive index n_g is a well-known function of the density of the gas [155], which was in turn calculated from the measured pressure and temperature using the equation of state, as described in Section IV G below.

The angle of incidence θ_i of the laser beam entering the pressure vessel could be varied continuously in the range $\pm 30°$, and was measured to an accuracy of $0.02°$ on a vernier-equipped scale. The large-angle scale and its vernier were ruled using a numerical milling machine. The angular locations of a sequence of interference minima were measured on both sides of $\theta_i = 0$. ¿From these measurements, and knowing n_g, θ_r can be calculated using Snell's law. The slope of a plot of $\cos \theta_r$ against the order number of the minima m (the unknown large, constant offset in m has no effect) is $\lambda / 2n_g d$, from which the cell thickness d can be determined with an uncertainty of ± 1 μm. Changes in the cell thickness (as distinct from its loss of parallelism, described above) resulting from large applied temperature differences are easily measured with this interferometer, and measured changes were consistent with the expected thermal expansion of the bottom plate.

E. Filling Procedure

Experiments were typically performed at pressures of 20–50 bar. Before the cell was pressurized, the wet region of the pressure vessel was filled with deionized water. Air bubbles were removed from the water and from the less-accessible corners of the wet region, and the water was thoroughly degassed. Bubbles increase the effective compressibility of the water, and thus the distance the bellows must move as the system is pressurized.

After the water bath was filled, the pressure vessel was sealed, and the pressure in both the dry and wet regions of the vessel was reduced with a vacuum pump to about 100 mTorr. Both regions were then re-pressurized to just above atmospheric pressure by filling the dry region with the experimental gas. The pumping line to the wet region was connected to an extra volume of water which was siphoned back into the water bath in the pressure vessel each time it was re-pressurized, ensuring complete filling of the wet region with water. This procedure was repeated roughly five times, repeatedly flushing the dry region of the pressure vessel, including the convection cell, with the experimental gas. In the wet region, each pumpdown boiled and degassed the internal water bath. After a few pumping/repressurization cycles, a valve between the extra water volume and the internal bath was closed and the entire vessel brought to the working pressure by pressurizing the dry side only, with the pressure being communicated to the water bath by the bellows. The system was cycled between the atmospheric pressure and the working pressure a few times to further flush the gas in the dry region.

During experimental runs of several weeks' duration, a significant amount of CO_2 typically diffused through the O-rings into the water. Thus, precautions were necessary during de-pressurization to prevent excessive gas formation in the wet region from compressing the bel-

lows unduly. For this purpose, an electrical lead which made contact with the bellows at a certain level of compression was used to signal the operator that some pressure relief in the wet region was needed before further de-pressurization of the dry region.

F. Rotation about a Vertical Axis

One version of the apparatus was mounted on a rotating table with a vertical rotation axis so that the effect of a Coriolis force on the RBC system could be studied. [40] In that case, the electrical leads were brought out of the rotating system through slip rings [156]. The shadowgraph system was co-rotating with the convection cell, so that all images were in the rotating frame.

G. Flow Visualization and Image Analysis

In addition to providing a qualitative picture of the convective flow pattern and its dynamics, an appropriately implemented visualization scheme can also be used to obtain quantitative information. Flow visualization was accomplished using the well-known shadowgraph technique [5–15]. Qualitatively, this method is easily understood from the standpoint of geometrical optics, [13] although a quantitative evaluation given near the end of this section requires that the diffraction effects of physical optics [15] be taken into account. The shadowgraph technique uses the lateral index-of-refraction variations of an otherwise transparent medium to visualize the convection pattern. In the case of convection, the warm, upwelling fluid has a lower index of refraction than the cool, down-flowing fluid. A parallel beam of light passing through the convecting fluid will be refracted by the convection rolls, and focused toward the regions of higher refractive index. In effect, the convection rolls act as an array of lenses, and when the beam of light impinges upon a screen, or, as in our experiments, on the ccd array of a video camera, regions of downflow appear bright, and regions of upflow appear dark. We visualize the convection from above, and the light and dark regions in the shadowgraph image have the same planform as the index variations, averaged over the thickness of the cell.

The sensitivity of the method depends upon the optical distance z_1 between the convection cell and the screen, and for sufficiently small z_1 increases with z_1. Under optimal circumstances, it can be very high. Measurements of the index-of-refraction variation with a resolution of 1 part in 10^9, corresponding to temperature variations of a few μK, have been made for convection in liquids where the refractive index n has a relatively large temperature coefficient

$$n_T \equiv -(\partial n/\partial T)_P \ , \tag{6}$$

of order 10^{-4} K^{-1} [157]. With image division (to be discussed below), it is then possible to observe convection patterns extremely close to onset, well before the flow has any measurable effect on the heat transport across the layer. However, the low refractive index of gases makes flow visualization relatively difficult at atmospheric pressure, and is one of the reasons for working at higher pressure. At 1 bar, one has $n_T = \mathcal{O}(10^{-6} \ K^{-1})$ and the effective focal length of the convective pattern is on the order of hundreds of meters. In order to get useful resolution, the screen would have to be placed inconveniently far from the convection cell. This is precisely what was done in the pioneering work of Ref. [102] mentioned in Sect. III, where the screen was placed 17 m beyond the cell! Under these conditions, however, diffraction severely limits the spatial resolution possible. On the other hand, at 30 bar, n_T is typically $10^{-4} \ K^{-1}$, the effective focal length of the pattern is of order 1 m, and very high resolution can be achieved at moderate distances.
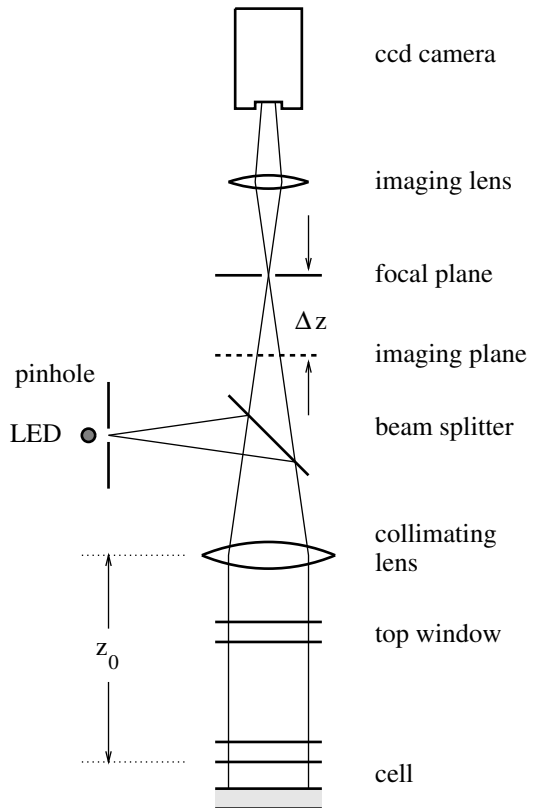

FIG. 13. Schematic diagram of the shadowgraph optics.

In order to make the apparatus versatile, it includes two lenses which, depending on their relative position, permit effective optical viewing distances z_1 which cover a very wide range. The optics is shown schematically in Fig. 13, and the shadowgraph tower is shown in Fig.

17

14. The system was contained in a cylindrical aluminum tower which was attached to the top flange of the pressure vessel during an experiment. Light from a "point source" was directed down onto the convection cell by a pellicle beam splitter. We used one of several achromatic lenses, most with a diameter of 10.2 cm, with a focal length in the range from 24 to 64 cm, to collimate the light beam which then passed through the thick window in the top flange, through the transparent cell top plate, and into the cell. The light was then reflected from the cell bottom plate and returned to the optics tower, having passed twice through the fluid layer. It was re-focussed by the collimating lens and imaged by a Nikon camera lens onto a ccd video camera.

The light source for the shadowgraph should ideally be monochromatic, to avoid chromatic aberrations in the optics and dispersion in the fluid. However, if the light source is spatially and temporally coherent, interference fringes are produced which obscure the shadowgraph effect. Light-emitting diodes, which produce incoherent light in a narrow frequency band of width approximately 100 Å, were found to be an excellent compromise.
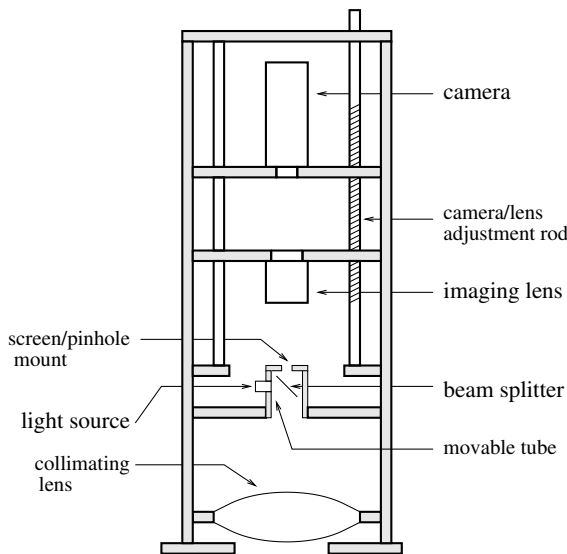

FIG. 14. The arrangement of components in the shadowgraph tower. The assembly is described in detail in the text.

One source we used was a bright LED [158], the surface of which was polished until the cathode wire was almost exposed. A 45 μm diameter pinhole [159] was then glued onto the surface over the LED element. A disadvantage of this technique is that the resulting illumination is not perfectly spatially uniform. The pinhole projects onto the cell an image of the LED chip, which has a dark spot (from a solder joint in the LED) in the center.

In more recent experiments, we used an LED coupled to a 50 μm graded-index silica fiber. The light was coupled into the fiber by drilling a hole, just large enough to accommodate the fiber and its cladding, in the plastic of the LED, extending to within 0.2 mm of the cath-

ode wire. The end of the fiber was glued into the hole with Epotek 301 epoxy [160], which has a refractive index closely matching that of silica. The fiber was then loosely coiled to scramble the image of the LED element. The other end of the fiber was polished and used as the light source. In addition to providing a more uniform source, the fiber also reduces the amount of light which misses the collimating lens and is lost. Very recently, we found a commercial source of a similarly-designed LED-fiber combination which is very convenient to use [161]. In order to get enough intensity, we often operated the LEDs above their rated current, up to 120 mA, without obvious detrimental effects. This was likely due to the improved heat sinking provided by our mount.

In some experiments the light source was an inexpensive laser diode operating at 780 nm [162]. The laser diode could be used without a pinhole, since the active area was only 20 μm by 60 μm, and it was extremely bright. It was typically used just below the laser threshold, where it was already several times brighter than the LED. The coherence length of this laser was sufficiently short that no interference fringes due to reflections between the top and bottom of the cell were observed, but the light was sufficiently coherent across the wavefront that interference rings due to dust in the optics were visible. At 780 nm, the laser diode was dimly visible to the eye for alignment purposes, and was in the wavelength range where the ccd camera is quite sensitive. The intensity of the laser was feedback controlled using its internal photodiode.

The light entering the convection cell should be collimated, so the light source must be positioned at the focal point of the collimating lens. To accomplish this, the source and beam splitter were mounted together on a tube which could be moved up and down (see Fig. 14). The lower part of the shadowgraph, including the collimating lens and the light source/beam splitter tube, was placed on a flat granite table with a plane mirror positioned just below the lens. A screen was placed over an aperture at the top of the tube, at the same distance from the beam splitter as the light source. The position of the tube was then adjusted until the image of the source on the screen was sharply focused. After this collimation procedure, the horizontal position and inclination of the collimating lens was adjusted so that the focused spot was centered on crosshairs inscribed on the screen. The lower half of the shadowgraph was then mounted on top of the pressure vessel. To insure that the shadowgraph axis was perpendicular to the cell, the shadowgraph tube was leveled so that the focused spot, now reflected from the cell bottom plate, was again centered on the cross hairs.

The optical path of the shadowgraph is illustrated in Fig. 13. The signal in the camera was generated by imaging a plane a distance Δz below the focal plane of the collimating lens onto the CCD element. From geometrical optics one sees that this is equivalent to viewing a shadowgraph signal which, in the absence of the colli-

mating lens, would have formed at an optical distance

$$z_1 = z_0 + \frac{f(f - \Delta z)}{\Delta z} \qquad (7)$$

from the cell. Here f is the focal length of the collimating lens (typically 50 cm), and $z_0 \simeq 20 \; cm$ is the optical distance from the sample to the collimating lens including corrections for the refractive indices of the water and windows in the optical path. Typical values of Δz are in the range 4 to 25 cm, giving values of z_1 in the range 500 to 50 cm. The value of z_1 affects the sensitivity as we will see below. For a given sensitivity, the magnification of the system can still be adjusted by changing the focal length of the imaging lens and the relative locations of the camera and the imaging lens, keeping the imaging plane fixed.

Values of Δz are not limited to the typical range given above. When Δz is such that a real image of the cell is formed on the detector, z_1 and thus the sensitivity of the shadowgraph is zero. One can observe a shadowgraph of the convection pattern when the optical system is focused either above or below the plane of the cell. These two shadowgraphs are negatives of each other, with the one formed by imaging a plane above the cell corresponding to Eq. 7 with $z_1 > 0$. For the shadowgraph to be linear (i.e., for Eq. 12 below to be a good approximation), care must be taken to avoid working near caustics, i.e., to avoid imaging planes for which z_1 is close to the effective focal length of the convection pattern. The zero-sensitivity condition — with the cell focused on the ccd detector — was often used as a starting point for the adjustment of the shadowgraph to higher sensitivity, and the sensitivity and magnification were adjusted by changing the positions of the ccd camera and imaging lens and the distance between them, without changing the alignment of the components in the lower half of the shadowgraph tube. An alternate procedure was to first focus the camera lens on the focal point of the collimating lens, corresponding to $\Delta z = 0$. The camera together with its lens was then lowered through the desired distance Δz. Depending on the sensitivity and magnification requirements, a 50 mm or a 35–70mm zoom Nikon camera lens was used as the imaging lens.

For quantitative analysis of the shadowgraph images, the optical system was calibrated. The combined response of the ccd camera and the video frame grabber which converted the camera output to digital format was calibrated using a set of neutral-density filters. Images without convection were digitized under different filters, and the average pixel intensities of a few different regions were compared. It turned out that the response of the ccd/digitizer system was sufficiently linear that only two parameter emerged from the calibration: the gain and the zero value, i.e., the average value for an image taken without light. This value was treated as an offset and subtracted from the images before image division.

After proper adjustment of the optics, we took images $\tilde{I}(\mathbf{x})$ which typically contained $m_0 = 256 \times 256 = 65536$

pixels (here $\mathbf{x}$ is the discrete horizontal position vector $\mathbf{x} = (i, j)$ within the cell). The light intensity at each pixel location was digitized in a range of 256 intensity levels, so as to be described by one byte of data. A background image $\tilde{I}_o(\mathbf{x})$ was taken at a value of ΔT well below the critical value ΔT_c for the onset of convection. Then ΔT was increased close to or above ΔT_c, and an image $\tilde{I}(\mathbf{x}, \Delta T)$ was taken at each value of ΔT which was of interest. The shadowgraph signal is then defined to be

$$I(\mathbf{x}, \Delta T) = [\tilde{I}(\mathbf{x}, \Delta T) - \tilde{I}_o(\mathbf{x})]/\tilde{I}_o(\mathbf{x}) \qquad (8)$$

where the division on the right-hand side of Eq. 8 corresponds to pixel-by-pixel division of the image matrices. This image division removes the dependence of I($\mathbf{x}$) on the system gain and also eliminates the effects of local inhomogeneities in the illumination or in the bottom plate reflectivity. For visual display, this signal was re-scaled so as to cover a suitable fraction of the range of integers between 0 and 255, and a corresponding grey-scale image was produced. Examples of such images have been given in Figs. 2, 3, and 4. For quantitative further analysis, $I(\mathbf{x}, \Delta T)$ was used directly.

Since runs of the experiments can last for several weeks, mechanical or thermal stresses in the shadowgraph tower can cause small misalignments between the data and background images. Shifts were small — typically from less than one to a few pixels. If the images were misaligned, the divided image showed a black or white line around the cell edge, and, for images recorded at small ϵ, imperfections on the cell bottom were highlighted. In the absence of a significant convection pattern, tool marks from the diamond machining of the bottom plate were discernible. The effects of the shift were largely eliminated by shifting the background to match the image. Shifts could be made with sub-pixel resolution by performing a bi-linear interpolation using the four nearest-neighbor pixels. Optimal shifts were determined by inspection of the edge of the cell in the divided image. For very weak signals, it often was possible to find the optimal shifts by minimizing the variance of the signal $I(\mathbf{x})$. This was so because the major contribution to the signal came from bottom-plate imperfections which divided out almost completely when the image and reference were properly aligned.

The shadowgraph images of convection very near threshold are often extremely faint. They can be enhanced by the use of Fourier filtering. Since the convection pattern has a characteristic length scale which is set by the cell thickness, a two-dimensional Fourier transform will have most of its power concentrated on a ring or in several spots corresponding to a wave number close to the critical wave number, k_c. Noise at low wave numbers is primarily due to large-scale imperfections in the optical quality of the cell bottom-plate which were not completely removed by the image division process, while high-k noise is mostly due to electronic noise in the video camera and the frame-grabber amplifier. By multiplying

the Fourier transform by a band-pass filter centered on k_c, one can eliminate much of this noise, and an inverse transform of the filtered Fourier transform yields an image with a much clearer pattern. Care must be taken to taper the filter edges gradually to prevent ringing which might introduce spurious structures into the image.
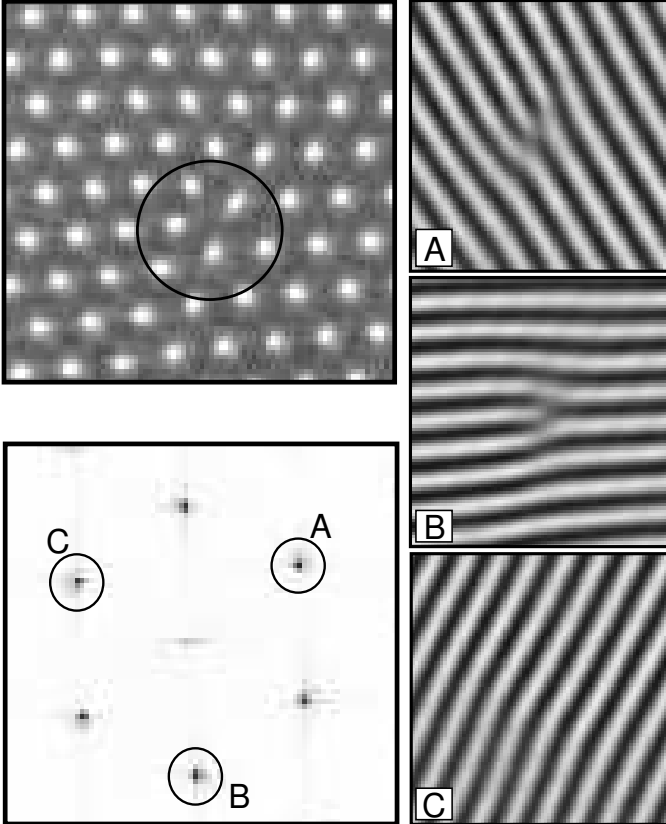

FIG. 15. A hexagonal pattern with a defect is shown in the upper left. The lower right is the modulus of the Fourier transform of this pattern. One sees that it is the sum of the Fourier transforms of three sets of rolls. The right three panels are the inverse tronsforms of the contributions from each of these sets of rolls. Two of these contain the defect, and the third does not.

One can also use this technique to create special-purpose filters, as illustrated in Fig. 15. The upper left part of the figure shows a shadowgraph image of a pattern of hexagonal convection cells containing a defect (the defect is located inside the circle). The modulus of the two-dimensional Fourier-transform $F(\mathbf{k})$ of the image is shown in the lower left of Fig. 15. It shows that a hexagonal pattern can be viewed as a superposition of three straight-roll patterns oriented at 120° with respect to each other, each contributing a pair of peaks. If one filters out all but one pair of peaks at $\mathbf{k}$ and $-\mathbf{k}$, corresponding to one of the three roll patterns, and then performs an inverse transform, one of the three straight-roll patterns is reconstructed. Figures 15(a–c) show the three roll patterns which make up the hexagonal pattern

of Fig. 15. This analysis shows that the defect in the hexagonal pattern is equivalent to dislocation defects in two of the three straight-roll patterns which combine to make up the hexagonal pattern. It is also possible to use this and related methods to determine the location of the defect, and to study the defect dynamics by following it as a function of time. Clearly, in a hexagonal lattice this dynamics must involve a combination of climbing (motion of the defect parallel to the roll axis) and gliding (motion perpendicular to the roll axis).

Another technique which we used was to filter out all but a single Fourier peak and then to translate this peak to $k = 0$. An inverse transform then yields a complex map of the slowly-varying amplitude of the pattern as a function of position, but with fast variations due to the individual convective rolls removed. Zeros of this function correspond to defects of the pattern. This technique works well for well-organized patterns such as the hexagonal array of cells shown in Fig. 3, but not for disordered patterns with many curved rolls and defects like that in Fig. 4.

A variety of other analyses of $F(\mathbf{k})$ have turned out to be useful [34,41]. These have included calculations of the azimuthal average $F(k)$ or the radial average $F(\Theta)$ of $F(\mathbf{k})$. The first moment of the structure factor $S(k) = |F(k)|^2$ gives a good estimate of the average wave number $\bar{k}$ of the pattern, and the second moment yields information about the wave number distribution or the inverse of the correlation length. "Contour plots" which give $|F(k)|$ or $|F(\Theta)|$ in the form of grey-scale plots as a function of time have been very useful in the study of the dynamics of patterns [41].

So far we have discussed primarily how to extract information regarding the pattern, or equivalently about the wave vector field. It is also possible to obtain quantitative information about the *amplitude* of the signal and to relate this to the amplitude of the temperature field. Let us write the deviation of the refractive index $n(\mathbf{x}, z, \Delta T)$ from the horizontally-uniform pure-conduction profile as

$$\delta n(\mathbf{x}, z, \Delta T) = \delta n(\mathbf{x}, \Delta T) f(z) \qquad (9)$$

where $f(z)$ is chosen so that its vertical average is equal to unity. On the basis of geometrical optics [8,9,12–15] one has

$$\frac{\tilde{I}(\mathbf{x}, \mathbf{\Delta T})}{\tilde{I}_0(\mathbf{x})} = (1 + 2z_1 d \nabla_h^2 n(\mathbf{x}))^{-1}. \qquad (10)$$

Here the factor of 2 comes from the light passing twice through the cell, and ∇_h^2 is the horizontal Laplacian. Eq. 10 is valid for z_1 much less than the geometric focalization length z_F at which Eq. 10 first predicts an divergent signal. For a superposition of spatially-sinusoidal refractive-index variations of uniform wave number q and to linear order, this gives

$$I(\mathbf{x}, \Delta T) = \mathcal{A}\, \delta n(\mathbf{x}, \Delta T) \qquad (11)$$

for the shadowgraph signal. The sensitivity $\mathcal{A}$ is given by

$$\mathcal{A} = 2d\gamma_1\gamma_2 q^2 z_1 . \tag{12}$$

In the formula derived from geometrical optics, [11,13] the coefficients γ_1 and γ_2 are equal to unity. In that case, $\mathcal{A} \propto 1/d$ since q is proportional to $1/d$. A thinner cell would thus seem to provide a stronger signal. However, to some extent this is illusory. On the basis of physical optics and for an initially parallel beam generated from a point source, $\gamma_2 = 1$ and γ_1 is shown in Ref. [15] to be given by

$$\gamma_1 = \sin(Kz_1)/Kz_1 \tag{13}$$

where

$$K = q^2/2k , \tag{14}$$

and $k \simeq 9.7 \times 10^4$ cm^{-1} is the wave vector of the light. For a distributed source consisting of light emanating uniformly from a circular pinhole of finite diameter l, [15]

$$\gamma_2 = 2J_1(qz_1\Theta_a)/qz_1\Theta_a \tag{15}$$

where $J_1(x)$ is the first-order Bessel function of the first kind,

$$\Theta_a = l/2f , \tag{16}$$

with f the focal length of the lens which generates the pseudo-parallel beam from the pinhole source. The typical case $l = 45$ μm and $f = 0.64$ m gives $\Theta_a = 3.5 \times 10^{-5}$. Equations 12, 13, and 15 show that the shadowgraph signal has extrema as a function of z_1. These can be seen in Fig. 16, which gives the sensitivity $\mathcal{A}$ as a function of z_1 for cells with the typical thicknesses $d = 0.1$ cm and $d = 0.05$ cm, assuming the representative case $q = \pi/d$. We see that the maximum sensitivity actually *decreases* with decreasing d, contrary to the predictions based on geometrical optics [13] which would be given by straight lines in Fig. 16 with slopes equal to those of the curves at the origin. A derivation and more detailed description of the physical optics of the shadowgraph method is given in Ref. [15].
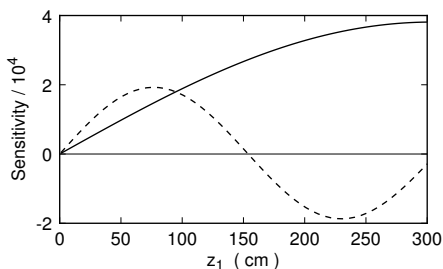

FIG. 16. Shadowgraph sensitivity $\mathcal{A}$ for a cell thickness $d = 0.1$ cm (solid line) and $d = 0.05$ cm (dashed line).

H. Gas properties

Much can be learned from heat-transport measurements and from an analysis of shadowgraph images without knowing the fluid properties. The distance from threshold can be defined in terms of the measured values of ΔT as $\tilde{\epsilon} \equiv \Delta T/\Delta T_c - 1$. The dependence of the Nusselt number on $\tilde{\epsilon}$ can be measured, and the evolution of pattern amplitudes and wavevector fields with $\tilde{\epsilon}$ can be studied in terms of the intensities of the Fourier components of the pattern without regard to the actual values of the temperature field. However, even more information can be extracted from the experiment when actual Rayleigh and Prandtl numbers are evaluated and when the actual temperature amplitudes are determined. [43,157] This requires a knowledge of some of the fluid properties. In addition, much theoretical work about RB convection [47] is based on the Oberbeck-Boussinesq approximation, [48,49] and the extent of the departures of a real physical system from this approximation can be evaluated only when the relevant properties are known as a function of temperature and pressure. Finally, in some of our work the coupling of external (thermal) noise to the hydrodynamic system has been of interest. This can be determined theoretically only when the viscosity and the Prandtl number are known. Thus we give in this section a summary of the properties of CO_2 which we have used in much of our work. We used this information over the range 10 to 60 °C and 20 to 60 bar.

For the density ρ we used Eq. 5.68 of Vukalovich and Altunin [163]. Since this equation is rather complicated, we do not reproduce it here. We obtained the isobaric thermal expansion coefficient

$$\alpha = -(1/\rho)(\partial\rho/\partial T)_P$$

from a numerical differentiation of the equation for ρ, using values of ρ at temperatures which were 0.1% of the absolute temperature ($\approx$ 0.3°C) below and above the mean temperature. Although usually not needed, we used a similar numerical procedure to get the isothermal compressibility.

The heat capacity was derived by bilinear interpolation in Table 3 of Angus et al. [164] We obtained the shear viscosity from a fit of the polynomial

$$\eta = \eta_{0,0} + \eta_{0,1}T + \eta_{0,2}T^2 + \eta_{1,1}\rho + \eta_{1,2}\rho^2 + \eta_{1,3}\rho^3 + \eta_{1,4}\rho^4$$

to the data of Iwasaki and Takahashi [165]. With T in K and ρ in g/cm^3, we found

$$\eta_{0,0} = -28.66 \times 10^{-6},$$

$$\eta_{0,1} = 0.6937 \times 10^{-6},$$

$$\eta_{0,2} = -3.455 \times 10^{-10},$$

$$\eta_{1,1} = 0.7352 \times 10^{-4},$$

$$\eta_{1,2} = 0.5813 \times 10^{-3},$$

$$\eta_{1,3} = 0.1751 \times 10^{-3},$$

and

$$\eta_{1,4} = 0.1137 \times 10^{-4},$$

when η is in Poise. This fit also agrees well with the data of Diller and Ball [166].

For the thermal conductivity, we fitted the data of Sengers [167] over the temperature range 298 to 323 K and the density range 0.0019 to 0.14 g/cm^3 to the function

$$\lambda = \lambda_{0,0} + \lambda_{0,1}T + \lambda_{0,2}T^2 + \lambda_{1,1}\rho + \lambda_{1,2}\rho^2 .$$

With T in Kelvin and ρ in g/cm^3, the coefficients

$$\lambda_{0,0} = 3165.24,$$

$$\lambda_{0,1} = -16.0129,$$

$$\lambda_{0,2} = 0.036625,$$

$$\lambda_{1,1} = 2867.92,$$

and

$$\lambda_{1,2} = 21137.7$$

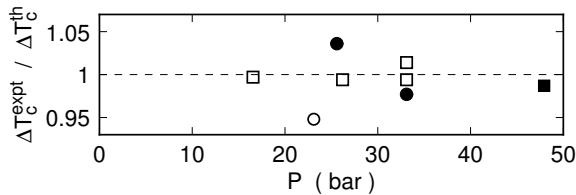give λ in erg/s cm K. Deviations from the fit are generally less than one percent [168].

FIG. 17. Ratio of the experimental to the theoretical values of ΔT_c. The different symbols refer to data taken in different apparatus.

As a test of the reliability of the fluid properties we determined the critical temperature difference for a number of different pressures and temperatures in cells of various spacings. The measurements spanned values of ΔT_c from 1.5 to 29 K, values of d from 0.05 to 0.2 cm, and pressures from 23 to 48 bar. Figure 17 gives, as a function of pressure, the ratio of $\Delta T_c^{expt}/\Delta T_c^{th}$ of the experimental ΔT_c to the ΔT_c calculated from the fluid properties, $R_c = 1708$, and the experimental pressure and mean

temperature. It can be seen that all experimental determinations are within a few % of the theoretical value, showing that the fluid properties are consistent with the experimental onset of convection.

Another useful parameter which we estimate from the fluid properties is the extent $\mathcal{P}$ of the departure from the Boussinesq approximation which was defined by Busse [55] and is given by him as

$$\mathcal{P} = \Sigma_{i=0}^4 \gamma_i \mathcal{P}_i ,$$

with

$$\gamma_0 = -\Delta\rho/\rho ,$$

$$\gamma_1 = \Delta\alpha/\alpha ,$$

$$\gamma_2 = \Delta\nu/\nu ,$$

$$\gamma_3 = \Delta\lambda/\lambda ,$$

and

$$\gamma_4 = \Delta C_P/C_P .$$

Here the quantities $\Delta\rho$, *etc.* are the difference in the value of the property at the bottom (hot) and top (cold) end of the cell. Good estimates of the coefficients in the equation for $\mathcal{P}$ are [55]

$$\mathcal{P}_0 = 2.676 - 0.1258/\sigma \simeq 2.54,$$

$$\mathcal{P}_1 = -6.603 - 0.5023/\sigma \simeq -7.13,$$

$$\mathcal{P}_2 = 2.755 \simeq 2.76,$$

$$\mathcal{P}_3 = 2.917 - 0.5023/\sigma \simeq 2.39,$$

and

$$\mathcal{P}_4 = -6.229 + 0.2512/\sigma \simeq -5.96.$$

Here the numerical values are for CO_2 at 25°C and 30 bar ($\sigma = 0.94$). Once $\mathcal{P}$ is known, the predicted ranges of stability of hexagons and rolls as well as the predicted amplitudes of the flow near the convective onset [31,47,55,118,169] are readily determined.

A further quantity of importance in some of the investigations is the parameter which gives a dimensionless measure of the strength of thermal noise, [170,171]

$$F_{th} = \frac{k_B T}{\rho d\nu^2} \times \frac{0.186\sigma^2}{\sigma + 0.5117} .$$

It also can be determined from the fluid properties given above.

Finally we mention that the quantitative determination of the temperature-field amplitude requires a knowledge of the refractive index n and its temperature derivative n_T. [43,157] These we calculated using the formula [172]

$$n = \sqrt{(1 + 2a_r\rho)/(1 - a_r\rho)}\,,$$

where $a_r = 0.152$ in the case of CO_2.

In Table I we give a few examples of typical parameter values for a mean sample temperature of $25°$ C. It is apparent that convection in gases is quite versatile. For instance the sample can have properties which conform well to the Boussinesq approximation, or it can show significant non-Boussinesq effects which lead to hexagons at onset. Another feature apparent from the Table is that the relative importance of thermal noise can be varied over a wide range. The values of $n_T = -(\partial n/\partial T)_P$ suggest that the sensitivity of the shadowgraph method can vary significantly.

TABLE I. Some properties of CO_2 relevant to convection.

P (bar)	d (cm)	ΔT_c ($°C$)	$10^4 \times n_T$ (K^{-1})	$\mathcal{P}$	$10^8 F$
10	0.2	4.33	0.170	0.24	1.56
20	0.1	6.07	0.441	0.50	7.1
30	0.05	14.2	0.900	1.68	24.9
40	0.03	21.8	1.79	4.49	69.0

V. RESULTS AND FUTURE PROSPECTS

Here we briefly describe and illustrate some interesting results obtained from experiments on RBC in compressed gases using the apparatus described above. More detailed accounts have been published elsewhere [31–44].

In a sense one of the most elementary aspects of convection, and yet from an experimental viewpoint one of the most difficult, is the study of fluctuations below the onset. Deterministic hydrodynamics predicts that there is a sharp bifurcation point below which the velocity field is zero. Above it, the amplitudes of the convective flow fields (in the Boussinesq approximation) are expected to grow in proportion to $\epsilon^{1/2}$. In reality, the effect of thermal noise on the system must be represented in the hydrodynamic equations by the addition of a stochastic stress tensor, as suggested by Landau and Lifshitz [173]. Well away from the bifurcation point, the effect of thermal noise on the system is expected to be very small because thermal noise is "microscopic" and the convection rolls are macroscopic; but as the onset of convection is approached, the susceptibility of the system to external disturbances diverges and at small ϵ even thermal noise has a significant influence. Patches of convection rolls are excited in random locations with random orientations and phases; their spatial extent on average is given by the correlation length $\xi = \xi_0/(-\epsilon)^{1/2}$ and their lifetime by the correlation time $\tau = \tau_0/(-\epsilon)$ ($\xi_0 = 0.385$ and $\tau_0 \simeq 0.077$ are length and time scales in units of d and t_v respectively). On average, the velocity field will be zero; but the root-mean-square average of the fluctuation amplitudes is predicted to diverge as $(-\epsilon)^{-1/4}$ until(at very small ϵ) nonlinear saturation effects keep it from growing further [174]. These fluctuations are the equivalent of critical opalescence near equilibrium critical points. One of the advantages of gas convection is that the effect of thermal noise can be made *relatively* large by an appropriate choice of experimental parameters [33,43]. In Fig. 18 we show experimental measurements of the mean-square temperature fluctuations below the onset of convection at two different pressures in CO_2 gas in a cell with $d \simeq 0.05cm$. The lines are the predictions [170,171] based on stochastic hydrodynamics [173]. As can be seen, the agreement between the measurements and the prediction based on thermal noise is excellent.
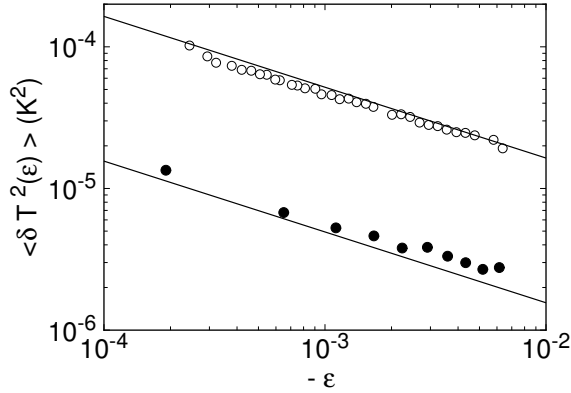
FIG. 18. The variance $\delta T^2(\epsilon)$ of the temperature fluctuations below the threshold for convection as a function of ϵ on logarithmic scales. •: P = 42.33 bar. ∘: P = 28.96 bar. The solid lines are the predictions fro m stochastic hydrodynamics based on thermal noise. After Ref. [43].

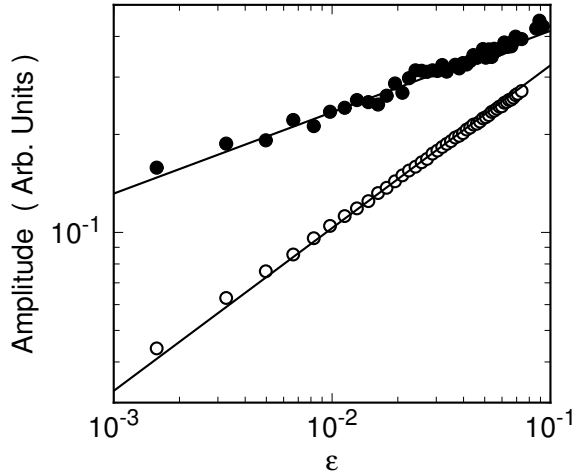FIG. 19. Amplitudes of convective flows as a function of ϵ. The origin of the ϵ-scale is based on the determination of ΔT_c from Nusselt-number measurements. Solid circles: amplitude of the umbilicus. Open circles: Amplitude of t he rolls away from the center. The lines have been drawn through the data with slopes corresponding to the predicted exponents. After Ref. [35].

Next we consider what happens just beyond the bifurcation point in a fluid which is described well by the Boussinesq approximation, i.e. one for which the fluid properties do not vary significantly over the height of the cell. When sidewall forcing is significant, a pattern of concentric rolls forms at the onset of convection [10,28,35,75] as is shown in Fig. 8. As ϵ is increased, the amplitude of the flow in the umbilicus at the center of the pattern initially grows faster than the amplitude away from the center. [76] This was explained theoretically by Pomeau et $al.$ [175], who predicted that the umbilicus amplitude should grow as $\epsilon^{1/4}$ whereas the roll amplitudes well away from the center should grow as $\epsilon^{1/2}$

[176]. Figure 19 shows experimental data from Ref. [35] which quantitatively support the predictions for these exponents.

As ϵ is increased, the first instability encountered by concentric-roll patterns is the focus instability, which involves a shifting off-center of the umbilicus of the pattern [10,28,35,177–182]. The focus instability (in the case of rigid sidewalls) was observed [35] at $\epsilon \simeq 0.16$, in quite good agreement with theoretical predictions [180]. Little is known theoretically about what should happen as ϵ is increased further; but from experiment there is a variety of sequences of events which seem to be sensitive to the aspect ratio Γ, and perhaps to the Prandtl number. For reasonably large Γ, the umbilicus initially can act as a source of rolls, emitting a traveling wave which moves radially in the outward direction [35]. However, when the umbilicus wanders further away from the center, its outward motion accelerates [35], presumably because it is influenced by the large-scale flow which becomes stronger as the deviation of the structure from circular symmetry is enhanced. As the umbilicus heads for the sidewall, it tends to compress the rolls which are in its path, causing them to form defects. Finally, the umbilicus arrives at the sidewall, where it turns into a wall focus. After some time, the curvature near the wall focus relaxes and a system of curved rolls develops, with the degree of curvature depending on the precise ϵ value. An example for $\epsilon = 0.115$ and $\Gamma = 41$ from Ref. [35] is shown in the top part of Fig. 20.

When ϵ is reduced to a small value for a pattern like that in Fig. 20, stable straight rolls with very little distortion like those in Fig. 2 are formed. Although they are stable close to onset, they become time dependent in an interesting way when ϵ is increased beyond about 0.08. This phenomenon was described in considerable detail by Croquette [28], and is illustrated in Fig. 20. As ϵ is increased, the increasing tendency for the rolls to terminate with their axes orthogonal to the sidewall [70,183] causes two grain boundaries or wall foci (depending on ϵ) to form, roughly on opposite sides of the cell. The remainder of the rolls then curve gently around these defects. The resulting curvature throughout the cell, and the associated large-scale flows, cause compression of the rolls in the cell center to the point where the local roll wavelength falls below a stability limit. A roll pair is "pinched off", leading to the formation of a defect pair. The two defects travel away from the center, reach and travel along the sidewall, and eventually are absorbed by the grain boundaries. The process then repeats itself, periodically or irregularly in time depending on Γ, ϵ, and σ. This process is illustrated in Fig. 20, where the mechanism of defect formation is the skewed-varicose instability [22,25]. In particular, the lower panels show that the instability is associated with a characteristic angle relative to the roll axes; this angle is close to that of the most unstable skewed-varicose disturbance [184]. The defects move, at least initially, in the direction determined by this angle, thus yielding a combination of climbing (mo-

tion parallel to the roll axes) and gliding (motion perpendicular to the roll axes). It is interesting to note that for the example of this process given by Croquette (Fig. 23 of Ref. [28]) the angle was close to zero and yielded a nearly pure climbing defect motion. Thus it seems that the mechanism in that case was not the skewed-varicose instability, but rather the Eckhaus instability [184].
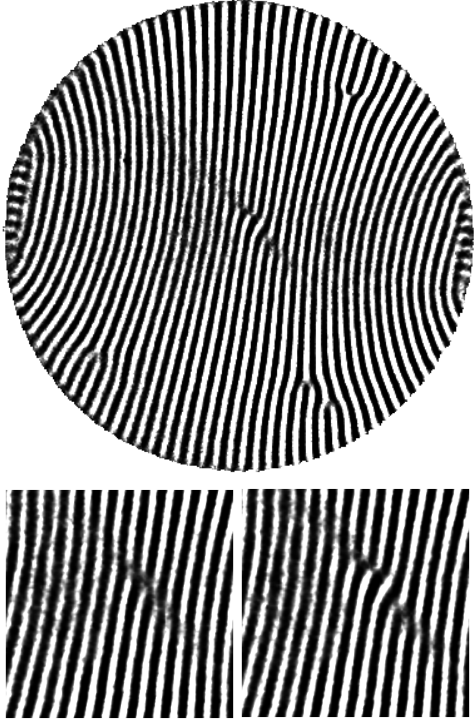

FIG. 20. A typical pattern of rolls at $\epsilon = 0.115$, where the sidewalls induce sufficient curvature to cause compression of the rolls in the center, which in turn leads to defect formation *via* the skewed-varicose mechanism. The lower two panels are enlargements of the center portion, at two times separated by $2.6 t_v$, and show the combination of climb and glide executed by the defect pair. After Ref. [35].

As ϵ is increased further, the average roll curvature increases as well. Wall foci form, such as can be seen in Fig. 4. Quantitative measurements of the average curvature and of the sidewall obliqueness have been made, [41], but the patterns are too complicated to yield to a detailed theoretical analysis at the present.

Under non-Boussinesq conditions, the initial pattern is predicted to consist of an array of hexagonal convection cells, which appear via a transcritical bifurcation [52–56]. Figure 3 shows a pattern of hexagonal cells recorded near onset [31] which agrees with this prediction. Here the cell thickness was only 0.52 mm and uniform to ± 0.5 μm. The aspect ratio was $\Gamma = 86$, and the fixed top plate temperature was 12.84 ± 0.05 °C. Under these conditions, ΔT_c was measured to be 29.026 ± 0.005 °C. The non-Boussinesq parameter was $\mathcal{P} = -3.4$. Convection first appeared as a localized patch of hexagonal cells in a region where ϵ was slightly greater than elsewhere. Then, as ϵ was increased, the pattern spread to fill the entire cell. Figure 3 shows an array of roughly 3500 hexagonal cells, with no internal defects, recorded at $\epsilon = 0.06$. The circular rolls at the perimeter of the cell are caused by the forcing due to the Macor sidewall (see Fig. 7(a)).
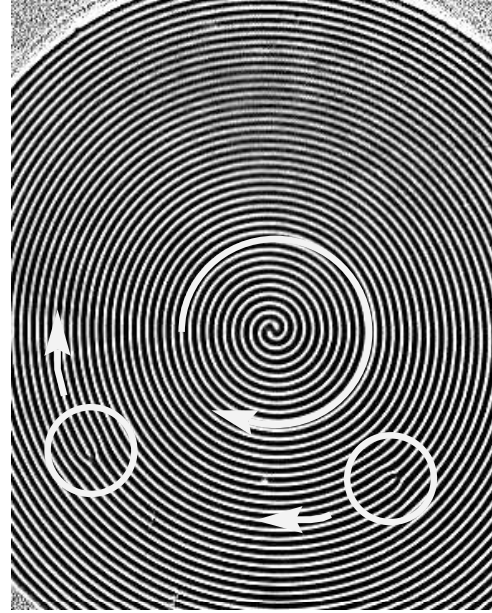

FIG. 21. A giant two-armed spiral at $\epsilon = 0.15$. The two arms terminate in defects which are circled in the figure. The structure rotates as indicated by the arrows, with a period of about 2400 t_v. After Ref. [31].

As ϵ was increased further, the hexagonal pattern became unstable and, after a long transient, was replaced by the pattern shown in Fig. 21 [31]. Here the convection takes the form of rolls, wound up into a giant spiral. The case shown in the figure has two arms, but spirals with from zero (a target pattern) to 13 arms were observed. Each arm terminates in a defect (circled in the figure), and the spiral heads and the defects rotate synchronously thus yielding a stable structure. The sense of rotation is such that the resulting waves propagate out from the spiral core. This state was unexpected, but has since been found in several numerical simulations of systems of equations which model RBC [185–188]. It appears to result from a coupling between the convective flow and large-scale flows. The structure is stabilized by the sidewall forcing caused by the Macor sidewalls used in these experiments; in the absence of this forcing it tends to drift off center, being destroyed in that process.
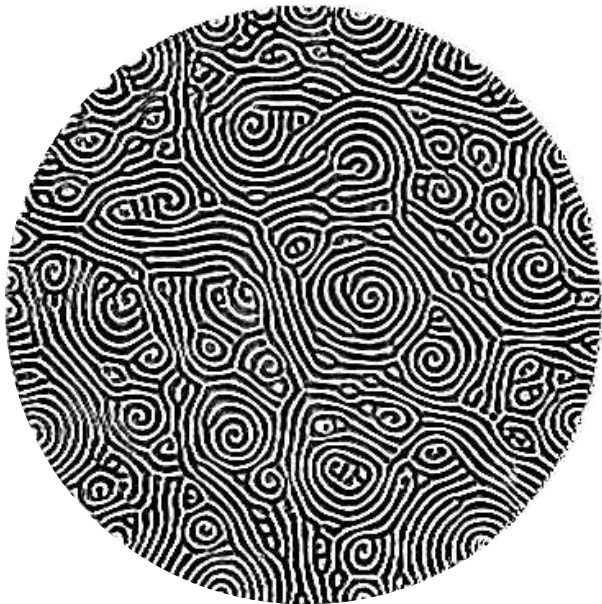
FIG. 22. An example of spiral-defect chaos for $\Gamma = 78$ and $\epsilon = 0.72$. After Ref. [34].

When ϵ was increased further using a large-aspect-ratio cell ($\Gamma = 78$), an unexpected new chaotic state was discovered for $\epsilon > 0.26$ [34]. It consists of a time-dependent pattern of many small spirals and other defects which are spontaneously created and destroyed. This state is a good example of the little-understood phenomenon of spatio-temporal chaos [1]. It is now referred to as spiral-defect chaos (SDC). Figure 22 shows a snapshot at $\epsilon = 0.72$ in a circular cell and with a nearly Boussinesq fluid. SDC has now been studied in a number of our investigations [34,35,37–39,41,44] as well as by others [74]. We found that this state occurs with square [42] as well as with circular sidewalls (provided the aspect ratio is large). Its occurrence is not sensitive to sidewall forcing, departures from Boussinesq conditions, or past history (*e.g.* whether ϵ is stepped to its final value or ramped quasistatically). More recently, we have shown [41,44] that the SDC state appears gradually (the time average of the number of spirals in a given cell increases smoothly from zero) from the roll state with sidewall foci or the straight-roll state which appears at the convective onset, and that the value of ϵ at the transition to SDC decreases as the aspect ratio Γ increases. Time series of shadowgraph images of this state were analyzed [42] by constructing the three-dimensional structure-factor $S(\vec{k}, \omega)$ (the modulus squared of the Fourier transform) of the shadowgraph intensity. These data were used to characterize the ϵ-dependence of the correlation length and time of the chaotic state [39,42]. Both were found to decrease approximately as a power law in ϵ, but a theoretical explanation of this behavior remains to be developed.

A similar chaotic state has since been found in several numerical models, including simulations based on a modified Swift-Hohenberg equation [189,190] and direct inte-

gration of the Navier-Stokes equations in the Boussinesq approximation [191]. In the simulations of Ref. [191], straight-roll solutions were only found when they were imposed as an initial condition. As a result of this work, it appears that both straight rolls and the SDC state coexist in the region of parameter space where it was previously believed that only straight rolls were stable. It also appears that SDC, and not the straight-roll state, is the "generic" state which is reached from almost all initial conditions.

A most fascinating aspect of SDC is its response to rotation of the convection cell about a vertical axis [44,184]. Let us define $M \equiv (n_r - n_l)/(n_r + n_l)$ with n_r and n_l equal to the average number of right-handed and left-handed spirals respectively. For rotation frequency $\Omega = 0$, one finds $M = 0$, indicating complete chiral symmetry. Rotation breaks this symmetry, yielding a function $M(\Omega)$ which tends to ± 1 as $|\Omega|$ grows. This function has a shape very similar to that of the magnetization of a paramagnet as a function of the magnetic field. It is interesting to speculate on the analogy between the statistical behavior of chaotic non-equilibrium systems and statistical-mechanical models for equilibrium phenomena.

The experiments which we described have demonstrated that convection in gases is a rich system for the study of patterns. New and unexpected phenomena, such as giant spirals and SDC, have been discovered as a direct consequence of the large aspect ratios which are accessible under a variety of experimental conditions. Work on this system is continuing on several fronts, and we mention briefly only a few of the as yet unexplored issues.

Much additional work is yet to be done on the effect of rotation on RBC [40,184]. Some of the interesting problems are the effect of rotation on the motion of defects, and on the SDC state. Another important project is the study of the Küppers-Lortz (KL) unstable state [192] which occurs immediately above the convective onset when Ω is large enough. The KL state is particularly interesting since it is an example of spatio-temporal chaos which is predicted to be entered from the conduction state *via* a supercritical bifurcation, near which a weakly-nonlinear theoretical approach should be applicable. A set of rolls is predicted to form which, once it acquires a finite amplitude, is unstable with respect to another set at an angle Θ close to $\pi/3$ to the original one. [192,193] Preliminary results of our work on this problem have been published; [32,40,44] but much remains to be done. The bifurcation was indeed found to be supercritical [184]. In Fig. 23 we show a typical pattern for $\Omega = 2\pi f d^2/\nu = 17.6$ (f is the rotation frequency in Hz) and $\epsilon = 0.024$. One can see that different parts of the sample contain more or less coherent rolls, with different roll patches having different orientations at a given time. As time evolves, the pattern constantly changes, with a given roll patch invading neighboring ones, mostly by front propagation. The right portion of Fig. 23 gives the modulus of the Fourier transform $F(\mathbf{k})$ of the image on the left. Consistent with the prediction that $\Theta \simeq \pi/3$,

a temporal sequence of $F(\mathbf{k})$ reveals three predominant roll orientations, two of which show up clearly in the case shown in Fig. 23. However, neither the time nor the length scale of the dynamics found in the experiments [40] is consistent with predictions based on theoretical models [194–196]. Thus, a complete understanding of this interesting state of spatio-temporal chaos is still elusive and much remains to be done both by experiment and in theory.
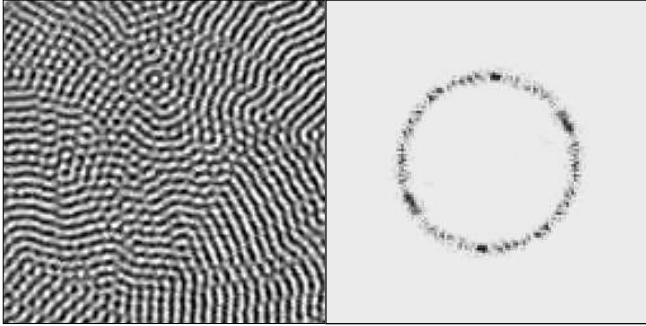

FIG. 23. An example of the Küppers-Lortz-unstable state for $\Gamma = 40$, $\Omega = 17.6$, and $\epsilon = 0.024$. The left part is the image in real space, and the right one is the modulus of the Fourier transform of this image. After Ref. [40].

An interesting variation of the KL problem is to study it in a system with strong deviations from the Boussinesq approximation where hexagons are observed for $\Omega = 0$. In that case it has been predicted [197,198] that the KL chaos should be replaced by a limit cycle; but experiments do not seem to exist as yet.

There are many additional problems of interest, of which we mention a few. For most of them, the large aspect ratio attainable in gases is important. One is convection in an inclined layer and is presently being studied in the group of one of us [199]. Another is the motion of defects in a hexagonal lattice where the topology requires that this motion be a combination of climb and glide (see Fig. 15). An interesting problem presently under study by part of our group is convection in gas mixtures [200], where parameter ranges [Lewis numbers of $\mathcal{O}(1)$, separation ratios from 0.01 to 1, and Prandtl numbers from 0.25 to 1], which are not accessible in liquid mixtures, can be explored. No doubt there are numerous other issues and problems which can be fruitfully investigated with the apparatus described in this paper.

ACKNOWLEDGMENTS

[1] For a comprehensive recent review, see M.C. Cross and P.C. Hohenberg, Rev. Mod. Phys. **65**, 851 (1993).

[2] H. Bénard, Rev. Gen. Sci. Pure Appl. **11**, 1261, 1309 (1900); and Ann. Chim. Phys. **23**, 62 (1901).

[3] A large literature pertaining to Rayleigh-Bénard convection has evolved. Particularly useful as introductions to early work are the reviews by E.L. Koschmeider, Adv. Chem. Phys. **26**, 177 (1974); and in *Order and Fluctuations in Equilibrium and Nonequilibrium Statistical Mechanics*, XVIIth International Solvay Conference, edited by G. Nicolas, G. Dewel, and J.W. Turner (Wiley, New York, 1981), p. 168; and by F. Busse, [23,16].

[4] G. Ahlers, in "25 Years of Nonequilibrium Statistical Mechanics", edited by M. Rubí (Springer, 1995).

[5] P.L Silveston, Forsch. Ing.-Wes. **24**, 29 (1958); 59 (1958). For a description of this early work, see also Sect. II.18 of Ref. [6].

[6] S. Chandrasekhar, *Hydrodynamic and Hydromagnetic Stability* (Oxford University Press, London, 1961).

[7] F.H. Busse and J.A. Whitehead, J. Fluid Mech. **66**, 67 (1974).

[8] W. Merzkirch, *Flow Visualization* (Academic, New York, 1974).

[9] R.J. Goldstein, *Fluid Mechanics Measurements* (Hemisphere, Washington, 1983).

[10] V. Steinberg, G. Ahlers, and D.S. Cannell, Phys. Script. **32**, 534 (1985).

[11] D. R. Jenkins, J. Fluid Mech. **190**, 451 (1988).

[12] V. Croquette, Contemp. Phys. **30**, 113 (1989).

[13] S. Rasenat, G. Hartung, B.L. Winkler, and I. Rehberg, Exp. Fluids **7**, 412 (1989).

[14] P. Kolodner and H.L. Williams in *Nonlinear Evolution of spatiotemporal structures in dissipative continuous systems*, edited by F.H. Busse and L. Kramer (Plenum, New York, 1990), p. 73.

[15] S. Trainoff, D.S. Cannell and G. Ahlers, to be published.

[16] F. Busse, in *Hydrodynamic Instabilities and the Transition to Turbulence*, edited by H.L. Swinney and J.P. Gollub (Springer, Berlin, 1981), p. 97;

[17] G. Ahlers, in *Lectures in the Sciences of Complexity*, edited by D. Stein (Addison-Wesley, Reading, 1989), p. 175.

[18] P. Manneville, *Dissipative Structures and Weak Turbulence* (Academic, San Diego, 1990).

[19] A.V. Getling, Sov. Phys. Usp. **34**, 737 (1991).

[20] G. Ahlers, in *Pattern Formation in Liquid Crystals*, edited by L. Kramer and A. Buka (Springer, 1995).

[21] F. Busse, J. Fluid Mech. **52**, 97 (1972).

[22] R. Clever and F. Busse, J. Fluid Mech. **65**, 625 (1974).

[23] F. Busse, Rep. Prog. Phys. **41**, 1929 (1978).

[24] F. Busse, J. Fluid Mech. **91**, 319 (1979).

[25] F.H. Busse and R.M. Clever, J. Fluid Mech. **91**, 319

(1979).

[26] F. Busse, J. Fluid Mech. **102**, 61 (1981).

[27] R.M. Clever and F.H. Busse, Phys. Fluids A2, 334 (1990).

[28] V. Croquette, Contemp. Phys. **30**, 153 (1989)

[29] F. Daviaud and A. Pocheau, Europhys. Lett. **9**, 7 (1989).

[30] A. Pocheau, J. Phys. (Paris) **49**, 1127 (1988); **50**, 2059 (1989).

[31] E. Bodenschatz, J.R. de Bruyn, G. Ahlers, and D.S. Cannell, Phys. Rev. Lett. **67**, 3078 (1991).

[32] E. Bodenschatz, D.S. Cannell, J.R. de Bruyn, R.E. Ecke, Y.-C. Hu, K. Lerman, and G. Ahlers, Physica **61D**, 77 (1992).

[33] E. Bodenschatz, S.W. Morris, J.R. de Bruyn, D.S. Cannell and G. Ahlers, in *Proceedings of the KIT Workshop on the Physics of Pattern Formation in Complex Dissipative Systems*, edited by S. Kai (World Scientific, Singapore, 1992), p. 227.

[34] S.W. Morris, E. Bodenschatz, D.S. Cannell, and G. Ahlers, Phys. Rev. Lett. **71**, 2026 (1993).

[35] Y. Hu, R.E. Ecke, and G. Ahlers, Phys. Rev. E **48**, 4399 (1993).

[36] L. Ning, Y. Hu. R.E. Ecke, and G. Ahlers, Phys. Rev. Lett. **71**, 2216 (1993).

[37] S.W. Morris, E. Bodenschatz, and J.R. de Bruyn, Phys. in Canada **50**, 9 (1994).

[38] Y. Hu, R.E. Ecke, and G. Ahlers, Phys. Rev. Lett. **72**, 2191 (1994).

[39] Y. Hu, R.E. Ecke, and G. Ahlers, Phys. Rev. Lett. **74**, 391 (1995).

[40] Y. Hu, R.E. Ecke, and G. Ahlers, Phys. Rev. Lett. **74**, 5040 (1995).

[41] Y. Hu, R.E. Ecke, and G. Ahlers, Phys. Rev. E **51**, 3263 (1995).

[42] S.W. Morris, E. Bodenschatz, D.S. Cannell, and G. Ahlers, unpublished.

[43] M. Wu, G. Ahlers, and D.S. Cannell, Phys. Rev. Lett. **75**, 1743 (1995).

[44] R.E. Ecke, Y. Hu. R. Mainieri, and G. Ahlers, Science **269**, 1704 (1995).

[45] Early efforts of determining the stable pattern immediately above the onset of convection include for instance the work of Malkus and Veronis. [46] A systematic study became available with the work of Schlüter, Lortz, and Bu sse. [47]

[46] W.V.R. Malkus and G. Veronis, J. Fluid Mech. **4**, 225 (1958).

[47] A. Schlüter, D. Lortz, and F. Busse, J. Fluid Mech. **23**, 129 (1965).

[48] A. Oberbeck, Ann. Phys. Chem. **7**, 271 (1879).

[49] J. Boussinesq., *Théorie Analytique de la Chaleur,* vol. 2 (Gauthier-Villars, Paris, 1903).

[50] K. Stork and U. Müller, J. Fluid Mech. **54**, 599 (1972).

[51] K. Stork and U. Müller, J. Fluid Mech. **71**, 231 (1975).

[52] E. Palm, J. Fluid Mech. **8**, 183 (1960).

[53] L. A. Segel and J. T. Stuart, J. Fluid Mech. **13**, 289 (1962).

[54] E. Palm, T. Ellingsen, and B. Gjerik, J. Fluid Mech. **30**, 651 (1967).

[55] F. Busse, J. Fluid Mech. **30**, 625 (1967).

[56] S. H. Davis and L. A. Segel, Phys. Fluids **11**, 478 (1968).

[57] G. Ahlers, Phys. Rev. Lett. **33**, 1185 (1974).

[58] G. Ahlers and R.P. Behringer, Phys. Rev. Lett. **40**, 712 (1978).

[59] R.P. Behringer and G. Ahlers, J. Fluid Mech. **125**, 219 (1982).

[60] R.P. Behringer, Rev. Mod. Phys. **57**, 657 (1985).

[61] S. Fauve, C. Laroche, and A. Libchaber, J. Phys. (Paris) Lett. **42**, 455 (1981).

[62] E. Siggia and A. Zippelius, Phys. Rev. Lett. **47**, 835 (1981).

[63] M.C. Cross, Phys. Rev. A **27**, 490 (1983).

[64] M.C. Cross and A.C. Newell, Physica **10D**, 299 (1984).

[65] A.C. Newell and J.A. Whitehead, J. Fluid Mech. **38**, 279 (1969).

[66] L.A. Segel, J. Fluid Mech. **38**, 203 (1969).

[67] Y. Pomeau and P. Manneville, J. Phys. (Paris) Lett. **40**, 609 (1979).

[68] H.R. Brand, in *Propagation in systems far from equilibrium*, edited by J.E. Wesfried, H. Brand, P. Manneville, G. Albinet, and N. Boccara (Springer-Verlag, Berlin, 1988), p. 206.

[69] G. Ahlers, D.S. Cannell, and V. Steinberg, Phys. Rev. Lett. **54**, 1373 (1985).

[70] M.S. Heutmaker and J.P. Gollub, Phys. Rev. A **35**, 242 (1987).

[71] A. Libchaber and J. Maurer, J. Phys. Lett. **39**, L-369 (1978).

[72] A. Libchaber and J. Maurer, J. Phys. (Paris) Colloque **41**, C3-51 (1980).

[73] M. Assenheimer and V. Steinberg, Phys. Rev. Lett. **70**, 3888 (1993).

[74] M. Assenheimer and V. Steinberg, Nature (UK) **367**, 347 (1994)

[75] E.L. Koschmieder and S.G. Pallas, Int. J. Heat Mass Trans. **17**, 991 (1974).

[76] V. Croquette, M. Mory, and F. Schosseler, J. Phys. (Paris) **43**, 293 (1983).

[77] C.W. Meyer, G. Ahlers, and D.S. Cannell, Phys. Rev. Lett. **59**, 1577 (1987).

[78] G. Ahlers, C.W. Meyer, and D.S. Cannell, J. Stat. Phys. **54**, 1121 (1989).

[79] G. Ahlers, Physica D **51**, 421 (1991).

[80] C.W. Meyer, G. Ahlers, and D.S. Cannell, Phys. Rev. A **44**, 2521 (1991).

[81] J.F. Harvey, *Theory and Design of Modern Pressure Vessels* (Van Nostrand Reinhold, New York, 1974).

[82] B. Castaing, G. Gunaratne, F. Heslot, L. Kadanoff, A. Libchaber, S. Thomae, X.-Z. Wu, S. Zaleski, and G. Zanetti, J. Fluid Mech. **204**, 1 (1989).

[83] E.H. Weber, Ann. Phys. Chemie **94**, 447 (1855).

[84] J. Thompson, Proc. Glasg. Phil. Soc. **13**, 464 (1882).

[85] H. Bénard, Revue générale des Sciences, **11**, 1261 (1900); *ibid.*, 1309 (1900); Thése de Doctorat, Paris (1901).

[86] J.R.A. Pearson, J. Fluid Mech. **4**, 489 (1958).

[87] M.F. Schatz, S.J. VanHook, W.D. McCormick, J.B. Swift, and H.L. Swinney, Phys. Rev. Lett. **75**, 1938 (1995).

[88] W. Nusselt, Forsch.-Arbeit auf dem Gebiete des Ing. Wesens, **Heft 63,64**, (1907).

[89] W. Nusselt, Gesundh.-Ing. **42,43**, 477 (1915).

[90] H. Gröber, Fundamentals of Heat Transfer (McGraw-Hill, New York, 1961).

[91] W. Mull and H. Reiher, Gesundh. Ing. Beiheft **28** Reihe 1, 1 (1930).

[92] J.G.A. De Graaf and E.F.M. Van der Held, Appl. Sci. Res. **3**, 393 (1953).

[93] S. Mal and G.T. Walker, Quart. J. Roy. Met. Soc. **57**, 413 (1931).

[94] A.C. Phillips and G.T. Walker, Quart. J. Roy. Met. Soc. **58**, 23 (1932).

[95] A. Graham, Phil. Trans. Roy. Soc **A232**, 285 (1933).

[96] L.A. Segel and J.T. Stuart, J. Fluid Mech. **13**, 289 (1962).

[97] Lord Rayleigh, Phil. Mag. **32**, 529 (1916).

[98] H. Jeffreys, Phil. Mag. **2**, 833 (1926); Proc. Roy. Soc. **A118**, 195 (1928).

[99] K. Chandra, Proc. Roy. Soc. Lond. **A164**, 230 (1938).

[100] D.T.E. Dassanayake, Ph.D. Thesis, Imperial College, London, 1939 (unpublished), cited in Ref. [101].

[101] O.G. Sutton, Proc. Roy. Soc. Lond. **A204**, 297 (1950).

[102] R.J. Schmidt and O.A. Saunders, Proc. Roy. Soc. Lond. **A165**, 216 (1938).

[103] O.A. Saunders and M. Fishenden, Engineering **139**, 483 (1935).

[104] H. Bénard and D. Avsec, J. Phys. Radium **9**, 486 (1938).

[105] D. B. Thomas and A.A. Townsend, J. Fluid. Mech. **2**, 473 (1957).

[106] J.W. Deardorff and G.E. Willis, J. Fluid Mech. **23**, 337 (1965).

[107] G.E. Willis and J.W. Deardorff, Phys. Fluids **8**, 2225 (1965).

[108] H.A. Thompson and H.H. Sogin, J. Fluid Mech. **24**, 451 (1966).

[109] J. Gille, J. Fluid Mech. **30**, 371 (1967).

[110] R. Krishnamurti, J. Fluid Mech. **42**, 295 (1970).

[111] R. Krishnamurti, J. Fluid Mech. **42**, 309 (1970).

[112] G.E. Willis and J.W. Deardorff, J. Fluid Mech. **44**, 661 (1970).

[113] G.E. Willis, J.W. Deardorff, and R.C.J. Somerville, J. Fluid Mech. **54**, 351 (1972).

[114] G. Ahlers, in *Fluctuations, Instabilities, and Phase Transitions*, edited by T. Riste (Plenum, NY, 1974), p. 181.

[115] G. Ahlers and R.P. Behringer, Prog. Theoret. Phys. Supplement **64**, 186 (1978);

[116] M.V.R. Malkus, Proc. Roy. Soc. A **225**, 196 (1954).

[117] R. Krishnamurti, J. Fluid Mech. **60**, 285 (1973); and references therein.

[118] G. Ahlers, J. Fluid Mech. **98**, 137 (1980).

[119] D.C. Threlfall, J. Fluid Mech. **67**, 17 (1975).

[120] L.M. Howard, in *Proceedings of the 11th International Conference on Applied Mechanics*, edited by H. Görtler (Springer, Berlin, 1964).

[121] H. Oertel, Jr. and K. Bühler, Int. J. Heat Mass Transfer **21**, 1111 (1978).

[122] H. Oertel, Jr. in *Flow Visualization II*, edited by W. Merzkirch (Hemisphere, Washington, 1980), p. 71.

[123] B. Martinet, P. Haldenwang, G. Labrosse, J.C. Payan, and R. Payan, J. Phys. (Paris) Lett. **43**, 161 (1982).

[124] B. Martinet, P. Haldenwang, G. Labrosse, J.C. Payan, and R. Payan, in *Cellular Structures in Instabilities*, edited by J.E. Wesfreid and S. Zaleski (Springer, Berlin, 1904), p. 33.

[125] J. Zirep and H. Oertel, *Convective Transport and Instability Phenomena* (Braun, Karlsruhe, 1982).

[126] J. R. Leith, in *Bifurcation Phenomena in Thermal Processes and Convection*, edited by H. Bau, L. Bertram, and S. Korpela (ASME AMD-Vol 89, New York, 1987), p. 91.

[127] J. R. Leith, Exp. in Fluids **5**, 354 (1987).

[128] J. R. Leith, Physica **37D**, 334 (1989).

[129] A. Pocheau, V. Croquette, and P. Le Gal, Phys. Rev. Lett. **55**, 1094 (1985).

[130] V. Croquette, P. Le Gal, and A. Pocheau, Phys. Scr. **T13**, 135 (1986).

[131] V. Croquette and H. Williams, Phys. Rev. A **39**, 2765 (1989).

[132] B. Janiaud, E. Guyon, D. Bensimon, and V. Croquette, in *Nonlinear Evolution of Spatio-Temporal Structures in Dissipative Continuous Systems,* edited by F.H. Busse and L. Kramer (Plenum, New York, 1990), p. 45.

[133] B. Janiaud, A. Pumir, D. Bensimon, V. Croquette, H. Richter, and L. Kramer, Physica **55D**, 269 (1992).

[134] J. Lega, B. Janiaud, S. Jucquois, and V. Croquette, Phys. Rev. A **45**, 5596 (1992).

[135] J.-M. Flesselles, V. Croquette, and S. Jucquois, Phys. Rev. Lett. **72**, 2871 (1994).

[136] M. Gitterman and V. Steinberg, High Temperature (USSR) **8**, 754 (1970).

[137] M. Gitterman, Rev. Mod. Phys. **50**, 85 (1978).

[138] K.H. Mueller, G. Ahlers, and F. Pobell, Phys. Rev. B **14**, 2096 (1976).

[139] J. Keat, lab report, Princeton University, 1994 (unpublished).

[140] P. Kolodner, Phys. Rev. Lett. **66**, 1165 (1991).

[141] Mellor Optics, Providence, RI.

[142] Optical Filter Corp., Keene, NH.

[143] Macor machinable ceramic, Corning Glass Works, New York, NY.

[144] H. Schenk, Jr., *Fortran Methods in Heat Flow* (The Ronald Press Co., New York, 1963); M. Necati Ozisik, *Boundary Value Problems of Heat Conduction* (International Textbook, Scranton, PA, 1968).

[145] Tokin Corp., San Jose, CA.

[146] Minco Products Inc., Minneapolis, MN.

[147] Fenwal Electronics Inc., Milford, MA.

[148] Conax Buffalo Corp., Buffalo, NY.

[149] Aquaclear Powerhead 800, Rolf C. Hagen Inc., Montréal, Canada.

[150] Emerson and Cuming, Inc., Woburn, MA.

[151] Sensotec, Columbus, OH.

[152] G.C. Straty and E.D. Adams, Rev. Sci. Instrum. **42**, 1393 (1969).

[153] F.A. Jenkins and H.E. White, *Fundamentals of Optics* (McGraw-Hill, New York, 1957).

[154] United Detector Technologies, Hawthorne, CA, model RTD 020 D.

[155] A.D. Buckingham, Proc. Roy. Soc. Lond. **A337**, 275 (1974).

[156] Fabricast, Inc., 2517 Seaman Ave, South El Monte, CA 91733

[157] M.A. Dominguez-Lerma, G. Ahlers, and S. Cannell, Phys. Rev. E, in print.

[158] Kilobright Light Emitting Diode, AND Div., W.J. Purdy Co., Burlingame, CA.

[159] M and W Systems, Hayward, CA.

[160] Epoxy Technology Inc., Billerica, MA.

[161] General Fiber Optics Inc., 1 Washington Ave, Fairfield, NJ 07004.

[162] Sharp Electronics, LT-022MC.

[163] M.P. Vukalovich and V.V. Altunin, *Thermophysical Properties of Carbon Dioxide* (Collets's, London, 1968).

[164] S. Angus, B. Armstrong, and K.M. de Reuck, *International Thermodynamic Tables of the Fluid State*, Vol. 3. Carbon Dioxide (Pergamon, Oxford, 1978).

[165] H. Iwasaki and M. Takahashi, J. Chem. Phys. **74**, 1930 (1981).

[166] D.E. Diller and M.J. Ball, Int. J. Thermophysics **6**, 619 (1985).

[167] J.V. Sengers, Ph.D. Thesis, University of Amsterdam, Netherlands, 1962 (unpublished).

[168] A more accessible and recent reference is B. Le Neindre, R. Tufen, P. Bury, and J.V. Sengers, Ber. Bunsen Ges. (Phys. Chem.) **77**, 262 (1973). We became aware of it only late in our work, and thus used our own fit to the original data of Sengers [167].

[169] S. Ciliberto, P. Coullet, J. Lega, E. Pampaloni, and C. Perez-Garcia, Phys. Rev. Lett. **65**, 2370 (1990).

[170] P.C. Hohenberg and J.B. Swift, Phys. Rev. A **46**, 4773 (1992).

[171] H. van Beijeren and E.G.D. Cohen, J. Stat. Phys. **53**, 77 (1988).

[172] A.D. Buckingham and C. Graham, Proc. R. Soc. Lond. A **337**, 275 (1974).

[173] L.D. Landau and E.M. Lifshitz, *Fluid Mechanics* (Pergamon, London, 1959).

[174] V.M. Zaitsev and M.I. Shliomis, Zh. Eksp. Teor. Fiz.**59**, 1583 (1970) [English Translation: Sov. Phys. JETP **32**, 866 (1971)].

[175] Y. Pomeau, S. Zaleski, and P. Manneville, Z. Angew. Math. Phys. **36**, 368 (1985).

[176] G. Ahlers, M.C. Cross, P.C. Hohenberg, and S. Safran, J. Fluid Mech. **110**, 297 (1981).

[177] V. Croquette, P. Le Gal, A. Pocheau, and R. Guglielmetti, Europhys. Lett. **1**, 393 (1986).

[178] A.C. Newell, in *Propagation in systems far from equilibrium*, edited by J.E. Wesfried, H. Brand, P. Manneville, G. Albinet, and N. Boccara (Springer, Berlin, 1988), p. 122.

[179] A.C. Newell, T. Passot, and M. Souli, Phys. Rev. Lett. **64**, 2378 (1990).

[180] A.C. Newell, T. Passot, and M. Souli, J. Fluid Mech. **220**, 187 (1990).

[181] A.C. Newell, T. Passot, and M. Souli, Eur. J. Mech. B/Fluids **10**, Suppl. 2, 151 (1991).

[182] V. Croquette and A. Pocheau, in *Cellular Structures and Instabilities*, edited by J. Wesfreid and S. Zaleski,

Lecture Notes in Physics Vol. 210 (Springer, New York, 1084), p. 106.

[183] M.C. Cross, Phys. Rev. A **25**, 1065 (1982).

[184] Y. Hu, R.E. Ecke, and G. Ahlers, to be published.

[185] M. Bestehorn, M. Fantz, R. Friedrich, H. Haken, and C. Pérez-Garcia, Z. Phys. B **88**, 93 (1992).

[186] M. Bestehorn, M. Fantz, R. Friedrich, and H. Haken, Phys. Lett. A **174**, 48 (1993).

[187] H. Xi, J. Gunton, and J. Viñals, Phys. Rev. E **47**, R2987 (1993).

[188] M. Bestehorn, M. Neufeld, R. Friedrich, and H. Haken, Phys. Rev. E **50**, 625 (1994).

[189] H. Xi, J. Gunton, and J. Viñals, Phys. Rev. Lett. **71**, 2030 (1993).

[190] M.C. Cross and Y. Tu, Phys. Rev. Lett. **75**, 834 (1995).

[191] W. Decker, W. Pesch, and A. Weber, Phys. Rev. Lett. **73**, 648 (1994).

[192] G. Küppers and D. Lortz, J. Fluid Mech. **35**, 609 (1969).

[193] R.M. Clever and F.H. Busse, J. Fluid Mech. **94**, 609 (1979).

[194] K.E. Heikes and F.H. Busse, Annals of the N.Y. Academy of Sciences **357**, 28 (1980).

[195] Y. Tu and M. Cross, Phys. Rev. Lett. **69**, 2515 (1992).

[196] M. Neufeld, R. Friedrich, and H. Haken, Z. Phys. B **92**, 243 (1993).

[197] A.M. Soward, Physica D **14**, 227 (1985).

[198] J.M. Rodríguez, C. Pérez-García, M. Bestehorn, M. Fantz, and R. Friedrich, Phys. Rev. A **46**, 4729 (1992).

[199] B. Plapp and E. Bodenschatz, unpublished.

[200] J. Liu, G. Ahlers, and D.S. Cannell, unpublished.